Title

Methionine oxidation activates pyruvate kinase M2 to promote pancreatic cancer metastasis

Journal

Molecular Cell, 82(16)

ISSN

1097-2765

Authors

He, Dan

Feng, Huijin

Sundberg, Belen

et al.

Publication Date

2022-08-01

DOI

10.1016/j.molcel.2022.06.005

Peer reviewed

HHS Public Access

Author manuscript

Mol Cell. Author manuscript; available in PMC 2023 August 18.

Published in final edited form as:

Mol Cell. 2022 August 18; 82(16): 3045–3060.e11. doi:10.1016/j.molcel.2022.06.005.

Methionine oxidation activates pyruvate kinase M2 to promote pancreatic cancer metastasis

Dan He[1], **Huijin Feng**[2,3], **Belen Sundberg**[2,3], **Jiaxing Yang**[2,3], **Justin Powers**[2,3], **Alec H. Christian**[1], **John E. Wilkinson**[4], **Cian Monnin**[5], **Daina Avizonis**[5], **Craig J. Thomas**[6,7], **Richard A Friedman**[3,8], **Michael D. Kluger**[9], **Michael A. Hollingsworth**[10], **Paul M. Grandgenett**[10], **Kelsey A. Klute**[11], **F. Dean Toste**[1], **Christopher J. Chang**[1,12,†], **Iok In Christine Chio**[2,3,13,†]

[1]Department of Chemistry, University of California, Berkeley, CA 94720, USA

[2]Institute for Cancer Genetics, Department of Genetics and Development, Columbia University Irving Medical Center, New York, NY 10032, USA

[3]Herbert Irving Comprehensive Cancer Center, Columbia University Irving Medical Center, New York, NY 10032, USA

[4]University of Michigan Medical School, Ann Arbor, MI 48109, USA

[5]Metabolomics Innovation Resource, Rosalind and Morris Goodman Cancer Institute, McGill University, Montreal, QC H3A 1A3, Canada

[6]Division of Preclinical Innovation, National Center for Advancing Translational Sciences, National Institutes of Health, Rockville, MD 20850, USA

[7]Lymphoid Malignancies Branch, Center for Cancer Research, National Cancer Institute, National Institutes of Health, Bethesda, MD 20892, USA

[8]Department of Biomedical Informatics, Columbia University Irving Medical Center, New York, NY 10032, USA

[9]Division of Gastrointestinal & Endocrine Surgery, Vagelos College of Physicians and Surgeons, Columbia University, New York, NY 10032, USA

[10]Eppley Institute for Research in Cancer and Allied Diseases, Fred & Pamela Buffett Cancer Center, University of Nebraska Medical Center, Omaha, NE 68198, USA

[†]Corresponding authors: chrischang@berkeley.edu (C.J.C.); christine.chio@columbia.edu (I.I.C.C.).

Author contributions: D.H., C.J.C, and I.I.C.C., conceived the study. D.H., H.F., and B.S. performed the experiments and analyzed the data. A.Y. and J.P. performed therapeutic dosing and tumor volume measurements. A.H.C. and F.D.T. provided Ox-alkyne probes. E.W. performed immunohistochemical scoring. D.A. and C.M. ran and analyzed ^{13}C-glucose experiments. C.J.T. provided TEPP46 and assisted with the analysis of metabolic experiments. R.F. performed bioinformatic analysis. M.D.K., M.A.H., P.M.G., K.A.K. collected patient-derived specimens. D.H., C.J.C, H.F., and I.I.C.C. interpreted the results and wrote the manuscript. All authors participated in discussing and finalizing the manuscript.

Declaration of Interests: C.J.C., F.D.T, and A.H.C. are inventors on patent applications related to the redox-active reagents for methionine conjugation. C.J.T. is listed as an inventor on patents related to PKM2 activators. The remaining authors declare no competing interests.

[11]Department of Internal Medicine, University of Nebraska Medical Center, Omaha, NE 68198, USA

[12]Department of Molecular and Cell Biology, University of California, Berkeley, CA 94720, USA

[13]Lead contact

SUMMARY

Cancer mortality is primarily a consequence of its metastatic spread. Here we report that methionine sulfoxide reductase (MSRA), which can reduce oxidized methionine residues, acts as a suppressor of pancreatic ductal adenocarcinoma (PDA) metastasis. MSRA expression is decreased in the metastatic tumors of PDA patients, while MSRA loss in primary PDA cells promotes migration and invasion. Chemoproteomic profiling of pancreatic organoids revealed that MSRA loss results in selective oxidation of a methionine residue (M239) in pyruvate kinase M2 (PKM2). Moreover, M239 oxidation sustains PKM2 in an active tetrameric state to promote respiration, migration, and metastasis, while pharmacological activation of PKM2 increases cell migration and metastasis *in vivo*. These results demonstrate that methionine residues can act as reversible redox switches governing distinct signaling outcomes and that the MSRA-PKM2 axis serves as a regulatory nexus between redox biology and cancer metabolism to control tumor metastasis.

Graphical Abstract

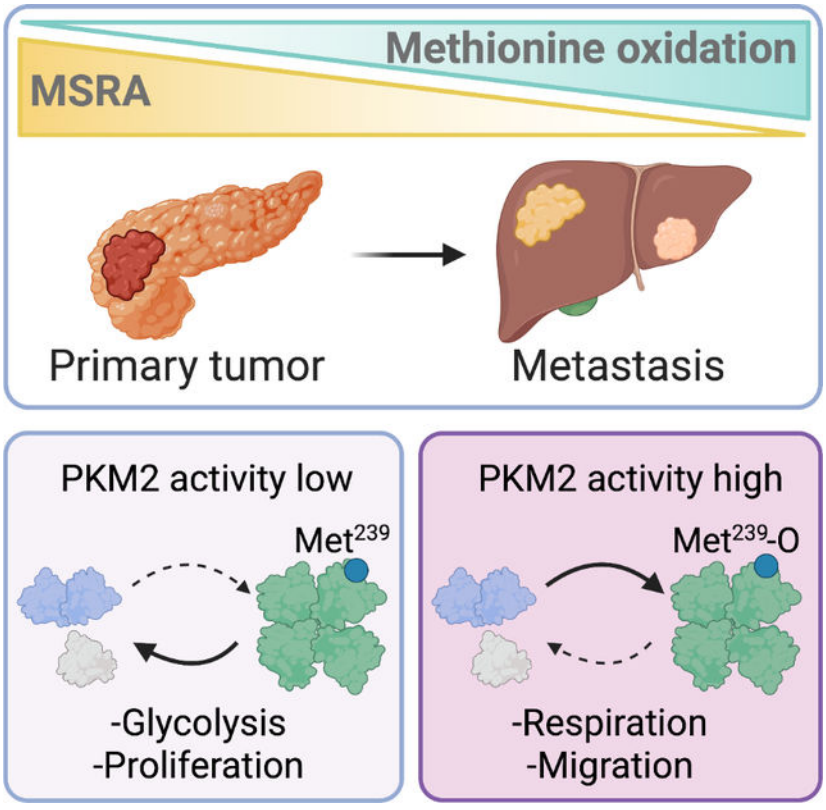

eTOC

He et al. identified a functional redox switch on pyruvate kinase PKM2 that is regulated by the methionine sulfoxide reductase, MSRA. Loss of MSRA promotes PKM2 methionine oxidation to increase respiration and metastasis. These findings implicate more sophisticated redox signaling mechanisms in tumorigenesis beyond oxidative stress.

Keywords

Redox signaling; methionine oxidation; pancreatic cancer; metastasis; cancer metabolism; glucose oxidation; PKM2

INTRODUCTION

Although reactive oxygen species (ROS) have been implicated in tumor development, the fundamental relationships between redox biology and cancer remain poorly understood (Reczek and Chandel, 2017). In addition to serving as indiscriminate oxidants that can irreversibly damage proteins, nucleic acids, and lipids, some ROS, such as H_2O_2, can regulate redox signaling through reversible oxidative post-translational modifications on cysteine residues (Paulsen and Carroll, 2013). For example, redox signaling through specific cysteines has been implicated in pancreatic ductal adenocarcinoma (PDA), the most common and lethal subtype of human pancreatic cancer. Greater than 95% of PDAs harbor pathogenic mutations of the KRAS proto-oncogene. Mutant KRAS signaling drives tumorigenesis in part by inducing Nrf2, a transcription factor that governs the cellular antioxidant response and elevates the levels of endogenous antioxidants (DeNicola et al., 2011). In doing so, Nrf2 induction sustains primary tumor growth by maintaining the reduced state of select cysteine sites within multiple translational regulatory factors (Chio et al., 2016). Thus, primary PDA tumor growth entails more sophisticated redox signaling mechanisms beyond indiscriminate oxidative damage. Nonetheless, it remains unclear whether distinct redox signaling mechanisms also contribute to the high metastatic potential of PDA and thus the dismal prognosis associated with this malignancy.

Whereas certain cysteine residues of protein are well-recognized as functional redox switches, less attention has been focused on methionine, the other sulfur-containing amino acid residue, and its reversible oxidation to methionine sulfoxide (Kim and Gladyshev, 2004; Stadtman et al., 2003). Two evolutionarily-related oxidoreductases, methionine sulfoxide reductase A (MSRA) (Moskovitz et al., 1995) and B (MSRB) (Moskovitz et al., 1997), serve as erasers of methionine sulfoxide post-translational protein modifications by reducing, respectively, methionine-*S*- and methionine-*R*-sulfoxide residues. Loss of MSR function is associated with a variety of age-related pathological conditions, including heart disease (Erickson et al., 2008), liver injury (Singh et al., 2017), and cancer (De Luca et al., 2010; Lei et al., 2007). More recently, the oxidation of specific methionine sites has also been implicated in cytoskeletal actin assembly (Hung et al., 2011; Lee et al., 2013) and phase separation (Kato et al., 2019). Nevertheless, it remains unclear whether methionine residues can also serve as physiological redox switches that cycle between oxidative and reduced states to regulate specific biological processes such as tumor development. To establish this concept, it will be necessary to identify specific methionine residues that can act as

redox switches, the regulatory factors that control their oxidation status, and the functional outcomes governed by their alternative redox states.

Our previous studies demonstrated that cysteine oxidation can suppress the formation of primary PDA tumors (Chio *et al.*, 2016). Here we show that loss of methionine sulfoxide reductase A (MSRA) drives the metastatic spread of PDA, suggesting that methionine-based redox signaling might regulate this process. Although substantial tools are available for profiling the redox-reactive cysteine proteome, analogous methods for methionine labeling under physiological conditions remain underdeveloped. Therefore, we applied a chemoselective bioconjugation approach to profile reactive methionines (Lin et al., 2017) in pancreatic ductal organoids established from different disease stages (Boj et al., 2015). By examining methionine oxidation of the proteome during PDA progression, we found that MSRA loss remodels glucose metabolism by allowing oxidation of a methionine residue (M239) that allosterically regulates pyruvate kinase M2 (PKM2). Interestingly, in contrast to cysteine-dependent oxidation that inhibits PKM2 activity (Anastasiou et al., 2011), methionine-based oxidation sustains PKM2 in an active tetrameric state to promote PDA cell mitochondrial respiration, migration, and metastasis.

RESULTS

MSRA suppresses pancreatic cancer metastasis

Immunohistochemical analysis of tissues from patient-derived pancreatic normal (N), primary tumor (PDA^T), and secondary liver metastasis (PDA^M) revealed that MSRA expression is reduced in primary tumor cells compared to adjacent normal tissue, and almost undetectable in liver metastases (Figures 1A and 1B, see Table S1 for subject characteristics). This expression pattern was also observed upon immunostaining pairs of murine PDA and liver metastasis tissues (Figure S1A) and immunoblot analysis of murine pancreatic ductal organoids (Figures 1C, 1D, and S1D). In contrast, normal, PDA^T, and PDA^M cells express comparable levels of MSRB1 and MSRB2 (Figures S1B and S1C). Decreased MSRA expression in PDA cells was not observed at the transcript level upon analysis of publicly available transcriptomic data from laser-capture microdissected human tissues (Figure S1E) (Moffitt et al., 2015) or from murine (Figure S1F) (Roe et al., 2017) or human (Figure S1G) (Tiriac et al., 2018) organoids. Using cycloheximide pulse-chase to measure the half-life of MSRA protein, we found that MSRA stability is decreased in tumor and metastatic organoids compared to normal counterparts (Figures S1H and S1I). Therefore, we examined the functional consequences of MSRA loss on pancreatic tumorigenesis using CRISPR-Cas9 to delete MSRA in murine PDA^T cells derived from KPC (*Kras*^{G12D}*; p53*$^{LOH/R172H}$*; PdxCre*) primary tumors (Hingorani et al., 2005) (Figure S1J). Genetic ablation of MSRA does not alter the expression of MSRB1 and MSRB2 (Figure S1J) and provides no growth advantage to PDA^T cells *in vitro* (Figures S1K to S1M) or *in vivo* upon orthotopic transplantation in syngeneic mice (Figures S1N). Strikingly, however, we observed a substantial increase in the incidence of metastasis (Figure 1E) to various organ sites (Figure S1O) by PDA^T cells upon MSRA deletion.

Interestingly, PDA^T organoids expressing a *MsrA*-specific sgRNA (PDA^T-sgMsrA) readily migrate through Matrigel and give rise to 2D monolayer outgrowths, unlike control

organoids (PDA^T-sgRosa) that maintain three-dimensional growth (Figures 1F and S1P). Moreover, two-dimensional PDA^T-sgMsrA cells display increased cell migration in wound-healing (Figures 1G and S1Q) and trans-well invasion (Figures 1H and S1R) assays. Conversely, ectopic expression of MSRA in PDA^T cells (Figure S1S) significantly suppresses cell migration (Figures 1I and S1T) and moderately suppresses cell proliferation (Figure S1U) *in vitro*. Notably, PDA^T-sgMsrA cells phenocopy the migratory behavior of PDA^M cells (Figure S1V), while *MsrA* deletion in PDA^M cells (PDA^M-sgMsrA) does not further accelerate migration (Figure S1V), presumably because basal MSRA expression in PDA^M cells is already very low (Figures 1C, 1D, and S1D). Consistent with these observations, we found that PDA^T-sgMsrA cells colonize the liver more efficiently than MSRA-expressing controls upon intrasplenic injection followed by splenectomy to model liver metastasis (Figures 1J to 1L, and S1W).

To further examine the tumor-suppressive functions of MSRA, we generated murine PDA^M cells to express MSRA in a doxycycline-inducible manner (Figure S1X). Dox-induced MSRA expression in murine PDA^M cells suppressed cell migration (Figure S1Y) with minimal impact on cell proliferation (Figure S1Z). To distinguish the contribution of MSRA to primary vs. metastatic tumor formation, we then examined the impact of Dox-induced MSRA expression on the behavior of PDA^M cells injected into either the pancreas or the spleen. Although MSRA induction does not affect the growth of established primary tumors injected into the pancreas (Figures S1AA to S1AC), it markedly reduces liver colonization when injected intrasplenically (Figures 1M to 1P, S1AD, and S1AE). Notably, whereas secondary macrometastases were observed in every mouse of the control (no Dox) cohort, none were observed in mice administered Dox immediately after transplantation (Figures 1Q to 1R). Collectively, these findings establish that the methionine sulfoxide reductase MSRA is a potent suppressor of pancreatic cancer metastasis.

Chemoproteomics identifies an enrichment of reactive methionine sites in metabolic enzymes

As oxidation of free and proteinaceous methionine has been shown to scavenge ROS (Luo and Levine, 2009), we asked whether downregulation of MSRA results in elevated global levels of ROS, which in turn might promote PDA metastasis by activating growth factor signaling pathways (Zhang et al., 2016). Using various approaches, we observed no increase in the global levels of free (reduced) methionine (Figure S2A), oxidized glutathione (Figure S2B), $NADP^+$ (Figure S2C), H_2O_2 (Figure S2D), or lipid ROS (Figures S2E and S2F) in PDA^T-sgMsrA cells. To ascertain whether MSRA contributes to compartment-specific alterations in redox homeostasis, we used roGFP2 biosensors expressed globally or specifically in the mitochondria (Morgan et al., 2011) to measure H_2O_2 and glutathione redox potential. Whereas metastatic PDA^M cells exhibit elevated mitochondrial H_2O_2 (Fig S2G), no detectable changes were observed in the mitochondrial H_2O_2 levels or glutathione redox potentials of PDA^T-sgMsrA cells (Figure S2H). Moreover, we observed no MSRA-dependent changes in 2,4-Dinitrophenylhydrazine (DNPH) labeling of global protein carbonylation (Figure S2I), an irreversible oxidative protein modification (Cattaruzza and Hecker, 2008). Thus, these collective observations indicate that downregulation of MSRA does not perturb global or mitochondrial ROS levels in PDA^T cells. Likewise,

MSRA deficiency does not activate effectors of the major signaling pathways implicated in metastasis (Salmeen and Barford, 2005), including the PI3K/AKT, MAPK, STAT, SMAD and AMPK cascades (Figures S2J to S2L). Furthermore, the gross morphology of F-actin organization (Figure S2M) and activities of focal adhesion proteins (Figure S2N) show no dependency on MSRA expression in PDA^T cells. Given these observations, we posited that MSRA suppresses PDA metastasis by controlling the oxidation state, and thus function, of a select group of protein targets.

To identify protein targets of methionine oxidation that underlie PDA metastasis, we used our chemoselective bioconjugation approach, termed redox-activated chemical tagging (ReACT) (Christian et al., 2019; Elledge et al., 2020; Lin *et al.*, 2017; Ohata et al., 2020), to profile for reactive proteinaceous methionine residues in pancreatic organoid models (Figure 2A). ReACT relies on an oxaziridine (Ox) warhead as a biomimetic nitrogen-transfer reagent to form stable protein-bound sulfoximines that are isoelectronic to methionine sulfoxide (Lin *et al.*, 2017). Installation of an alkyne handle (Ox-alkyne) further enables the sulfoximine (N-transfer) product to be biotin tagged for subsequent enrichment and proteomic analyses, whereas the sulfoxide (O-transfer) product is traceless (Figure 2A). To identify methionine oxidation events operant in different stages of PDA development, we coupled ReACT with quantitative proteomics to profile the reactive methionine proteome of pancreatic organoids (Figure 2B). Herein, methionine oxidation is defined by the loss of reactivity towards Ox-alkyne, as exemplified by the H_2O_2-dependent decrease in Ox-alkyne enrichment of known reactive methionine-containing proteins (Lin *et al.*, 2017) (Figure S2O). Reactive methionine sites from three biological replicates of murine N (normal), primary PDA^T ($Kras^{G12D}; p53^{LOH/R172H}$), and metastatic PDA^M ($Kras^{G12D}; p53^{LOH/R172H}$) organoids were enriched by Ox-alkyne-mediated conjugation (Figure 2B). By normalizing reactive methionine changes across the proteome, we were able to identify oxidative alterations in the methionine proteome independent of protein expression differences. From this experiment, 1103 reactive methionine-containing peptides, derived from 415 distinct proteins, were identified and quantified across all samples (Table S2). Reactive methionine-containing proteins constituted 30% of the identified proteins (1407 proteins have been identified and quantified from all samples). Comparing N, PDA^T, and PDA^M organoids, we found a significant decrease in protein-specific methionine reactivity, reflecting an increase in methionine oxidation, in both PDA^T and PDA^M organoids, with the most robust changes observed in the PDA^M setting (Figure 2C). This pattern of methionine oxidation is in direct agreement with the pattern of MSRA expression in human and murine pancreatic specimens (Figures 1A to 1D). Curiously, some methionine residues exhibit increased reactivity in both PDA^T and PDA^M organoids (Figure 2C). This observation may be due to conformational changes brought about by methionine oxidation that allow previously buried methionines to become solvent accessible and hence reactive to oxaziridine. Indeed, a recent study demonstrated similar biochemical alterations to cysteine reactivity due to local phosphorylation events (Kemper et al., 2022).

We identified 26 proteins in PDA^T (Table S3) and 147 proteins in PDA^M (Table S4) organoids that contain significantly oxidized methionines. To determine whether the subsets of methionine-oxidized proteins in PDA^T and PDA^M organoids represent particular biochemical processes, our datasets were subjected to KEGG pathway enrichment analysis

(Kanehisa et al., 2019). Interestingly, we found that the methionine-oxidized proteins are most highly enriched for participation in metabolic pathways in PDA^T organoids and, to a greater extent, in PDA^M organoids (Figure 2D). Indeed, more than half of the methionine-oxidized proteins from PDA^M organoids are involved in central carbon metabolism (Figures 2E and S2P). These results suggest that the cyclic oxidation and reduction of methionine residues on select proteins may constitute a regulatory mechanism that controls glucose metabolism in metastatic pancreatic cancer.

MSRA deficiency promotes oxidative phosphorylation of glucose in PDA models

To examine the functional consequences of such oxidative modifications, we performed Seahorse analysis on a panel of PDA^T cells that are either proficient or deficient for MSRA. Deletion of MSRA does not alter basal (Figure 3A) or stress-induced (Figure 3B) glycolysis in PDA^T cells, as measured by the extracellular acidification rate (ECAR). However, PDA^T-sgMsrA cells display increased basal (Figure 3C) and stress-induced (Figure 3D) mitochondrial oxidative phosphorylation (OxPHOS), as measured by oxygen consumption rate (OCR) in glucose replete (pyruvate and glutamine free) media. Conversely, doxycycline-induced expression of MSRA decreases basal OCR in both murine (Figure S3A) and human (Figure S3B, S3C) PDA cells. These changes are not due to alterations in mitochondrial mass (Figure S3D). Likewise, PDA^M organoids exhibit a significant increase in basal and stressed OCR (Figure 3E) compared to PDA^T organoids, with no difference in mitochondrial mass between the two groups (Figure S3E). In addition, stressed, but not basal, ECAR is increased in PDA^M compared to PDA^T organoids (Figure 3F). This result is consistent with our chemoproteomics data showing that GAPDH, the rate-limiting enzyme of glycolysis (Shestov et al., 2014), is not differentially oxidized in PDA^M organoids. Upon heavy isotope tracing of uniformly labeled $^{13}C_6$-glucose for 30 minutes, we observed a marked increase in ^{13}C-labeled pyruvate, but not its proximal glycolytic intermediates, in PDA^T-sgMsrA cells (Figure 3G). Whereas the levels of ^{13}C-lactate are not significantly increased in PDA^T-sgMsrA cells (Figure 3G), all downstream metabolites of the tricarboxylic acid (TCA) cycle display elevated ^{13}C labeling (Figure 3H), confirming that MSRA loss promotes glucose oxidation. Moreover, PDA^M cells exhibit increased ^{13}C-labeling of pyruvate (Figure 3I), and the TCA cycle intermediates (Figure 3J) compared to PDA^T cells, while deletion of MSRA does not further increase labeling in PDA^M cells (Figures 3I and 3J). Accordingly, PDA^T-sgMsrA (Figure 3K) and PDA^M (Figure 3L) cells generate more ATP from respiration than control PDA^T cells. As ATP is the main “energy currency” of the cell, elevated ATP synthesis likely serves to power the bioenergetics of cell migration. Indeed, localized ATP production has been shown to drive adaptive F-actin polymerization and invasion in various cell types (Kelley et al., 2019). In agreement with these observations, exposure of PDA^T cells to AZD7545, a selective PDK1/2/3 inhibitor that promotes pyruvate oxidation (Kato et al., 2007), increases both basal OCR (Figures 3M and S3F) and cell migration (Figures 3N and S3G) in an MSRA-dependent manner. Collectively, these observations suggest that MSRA contributes to this metabolic demand of metastatic PDA cells and that pyruvate kinase (PKM), which catalyzes the irreversible conversion of phosphoenolpyruvate and ADP to pyruvate and ATP (Israelsen and Vander Heiden, 2015), is a key metabolic node regulated by MSRA in these cells.

In addition to supporting bioenergetics through ATP synthesis, mitochondrial respiration also drives the production of aspartate (Birsoy et al., 2015; Cattaruzza and Hecker, 2008; Sullivan et al., 2015) and asparagine (Krall et al., 2021). PDA^{T}-sgMsrA cells contain higher levels of both aspartate (Figure S3H) and asparagine (Figure S3I), with the increase in aspartate arising through *de novo* synthesis from glucose, as evidenced by increased M+2 and M+3 ^{13}C labeling (Figure S3J). In contrast, the opposite phenotype was generated upon ectopic expression of MSRA in PDA^{T} cells (Figure S3K). In accordance with the role of aspartate as a precursor for nucleotide biosynthesis (Lane and Fan, 2015), PDA^{T}-sgMsrA cells exhibit increased steady-state (Figure S3L) and labeled (Figures S3M to S3P) nucleotide pools. A similar increase in *de novo* nucleotide synthesis was also observed when comparing PDA^{M} to PDA^{T} cells (Figures S3N and S3P), whereas no change in glucose contribution to the pentose phosphate pathway was detected in either PDA^{T}-sgMsrA cells or PDA^{M} cells relative to PDA^{T}-sgRosa cells (Figure S3Q). In accord with a previous report that the bioavailability of asparagine, a product of aspartate amidation, governs metastasis (Knott et al., 2018), we found that exposure of PDA^{T} cells to either exogenous aspartate (Figure S3R) or asparagine (Figure S3S) under non-proliferating conditions substantially increased cell migration *in vitro*. Collectively, our data indicate that loss of MSRA promotes glucose oxidation to support both the bioenergetic and biosynthetic needs of metastatic pancreatic cancer cells.

MSRA-dependent methionine oxidation activates PKM2

In accordance with metabolic tracer analyses indicating that glucose oxidation is increased in PDA^{M} (Figures 3I and 3J) and PDA^{T}-sgMsrA (Figures 3G and 3H) cells at the step of phosphoenolpyruvate conversion to pyruvate, chemoproteomic profiling of reactive methionines identified the pyruvate kinase muscle isozyme (PKM) as the most strongly oxidized metabolic enzyme in PDA^{T}-sgMsrA cells (Figure 4A). Thus, we next sought to decipher the biochemical regulation of PKM by MSRA. The increase in PKM methionine oxidation in PDA^{M} cells detected by mass spectrometry is further confirmed by immunoblotting for Ox-alkyne-reactive PKM (Figure 4B). Consistent with our metabolic observations, PKM activity is significantly higher in PDA^{M} cells compared to PDA^{T} counterparts (Figure 4C). To examine the direct relationship between PKM and MSRA, we first tested whether these proteins can interact in the cell. Indeed, MSRA was readily detected in PKM immunoprecipitates prepared from PDA^{T} cells that stably express an ectopic MSRA polypeptide (Figures 4D and S4A). Whereas MSRA deletion does not alter PKM protein expression in PDA^{T}-sgMsrA cells (Figure 4E), it significantly increases the methionine oxidation status of PKM, as reflected in the decreased PKM reactivity to Ox-alkyne observed by both immunoblotting (Figure 4E) and mass spectrometry (Figure 4F). MSRA deletion also increases pyruvate kinase activity in PDA^{T}-sgMsrA cells (Figure 4G), in accordance with our metabolic tracer analyses. Since ROS-induced oxidation of cysteine residue C358 can inhibit PKM2 enzymatic activity (Anastasiou *et al.*, 2011), we also examined the cysteine oxidation status of PKM2 and, as expected, no MSRA-dependent changes were detected by either iodoacetamide-alkyne labeling of free thiols (Figure S4B) and dimedone-alkyne (DYn-2) labeling of sulfenic acid (Figure S4C). Similar results were also observed in HEK293T cells expressing short-interfering RNAs (siRNA) against

MSRA (Figures S4D and S4E). These results indicate that MSRA regulates PKM activity independent of cysteine-based oxidation.

The mammalian PKM gene encodes two alternatively spliced products, PKM1 and PKM2, with very different enzymatic properties (Israelsen and Vander Heiden, 2015). Whereas PKM1 is constitutively active, the enzymatic activity of PKM2 is subject to complex allosteric regulation, with important implications for tumor progression and metastasis (Christofk et al., 2008a; Gruning et al., 2011; Guminska et al., 1997; Mazurek et al., 2005). To evaluate the impact of MSRA on the enzymatic activities of PKM1 and PKM2, each protein was ectopically expressed in PDA^T (Figures 4H and 4I) or HEK293T (Figures S4F and S4G) cells that do or do not express MSRA. As shown, immunopurified PKM2, but not PKM1, displayed increased pyruvate kinase activity upon MSRA depletion. Moreover, ectopically expressed PKM2 interacts with MSRA (Figure S4H), and PKM2 enzymatic activity is elevated in PDA^M cells (Figure 4J). Further, Ox-alkyne labeling confirms that PKM2 exhibits increased methionine oxidation upon MSRA deletion *in vitro* (Figures 4K and S4I) and *in vivo* (Figure S4J) with the oxidation status of resident cysteines unchanged in both PDA^T cells (Figure S4K) and HEK293T cells (Figures S4L and S4M). Thus, MSRA directly and selectively regulates PKM2 activity by modulating its methionine oxidation status.

Given that PDA^M cells have elevated mitochondrial H_2O_2 levels compared to PDA^T cells (Figure S2G), we asked if mitochondrial ROS is the source of PKM2 oxidation. Indeed, induction of mitochondrial ROS using inhibitors of complex I and complex III readily oxidizes reactive methionine on PKM2 within 30 minutes of treatment (Figure S4N), and the same level of oxidization was apparent for cysteine after 2 hours of treatment (Figure S4O). These data identify mitochondrial ROS as a source of PKM2 methionine oxidation. To ascertain whether antioxidants can reverse the methionine oxidation status of PKM2 and impede cell migration, we then examined the impact of *N*-acetylcysteine (NAC), a global antioxidant, or MitoTempo, a mitochondria-targeted superoxide dismutase mimetic, on PDA^T-sgMsrA cells. Surprisingly, these agents had no effect on either the methionine oxidation state of PKM2 (Figures S4P and S4Q) or the migration potential (Figures S4R and S4S) of these cells. Instead, we observed significant increases in the PKM2 methionine reactivity and migration potential of the control PDA^T-sgRosa26 cells. These results indicate that the enzymatically controlled redox signaling of PKM2 mediated by MSRA cannot be replaced by exogenous antioxidants.

Site-specific PKM2 oxidation on methionine 239 promotes tetramer formation

There are 16 methionine residues on PKM2. Based on our chemoproteomic analyses, six of these residues are redox-sensitive, but only methionine M239 exhibits a selective decrease in Ox-alkyne reactivity in PDA^M organoids (Figures 5A) and PDA^T-sgMsrA cells (Figure S5A), relative to PDA^T controls. Notably, of all the oxidized methionine-containing peptides identified in PDA^M organoids, the PKM-M239 peptide is the most strongly oxidized (Figure 5B). M239 is located proximal to a regulation hub that governs the allosteric transition of PKM2 by fructose-1,6-bisphosphate (FBP) (Macpherson et al., 2019) (Figure 5C), and is evolutionarily conserved (Figure 5D). Importantly, the replacement of M239, but not two

other surface-exposed residues (M149 and M494) (Figure S5A), with a redox-insensitive leucine abolishes the induction of PKM2 activity in PDA^{T}-sgMsrA (Figure 5E) and HEK293T cells (Figures S5B and S5C).

PKM2 is known to regulate its activity by switching between low-activity dimeric and high-activity tetrameric states, allowing cellular metabolism to shift between glycolysis and mitochondrial respiration, respectively (Mazurek *et al.*, 2005). Thus, we asked whether M239 oxidation of PKM2 regulates its oligomeric state. In support of this hypothesis, we observed that MSRA deletion enhances tetramer formation of endogenous PKM2 in PDA^{T} cells (Figure S5D) and PDA^{M} cells (Figure S5E) compared to control PDA^{T} cells. Importantly, this phenomenon was observed only with wild-type PKM2 protein (Figure 5F), but not with the PKM2-M239L mutant (Figure 5G). Using size exclusion chromatography to examine the molecular weight distribution of PKM2, we further confirmed that PDA cells deficient of MSRA enrich for high molecular weight PKM2 wildtype, but not M239L mutant, protein (Figure 5H). Similar results were observed in HEK293T cells (Figure S5F). These observations indicate that M239 oxidation promotes both the tetramerization and enzymatic activity of PKM2. Finally, to corroborate these results, we stimulated PKM2 activity using TEPP46, a PKM2-specific activator that promotes its tetrameric state (Jiang et al., 2010; Macpherson *et al.*, 2019) and confirmed that it promotes PKM2 activity (Figure S5G) by increasing its tetramerization (Figures S5H and S5I) in an MSRA-dependent manner. These changes in PKM2 oligomerization status do not alter its cellular distribution (Figure S5J). Taken together, these results confirm that the oxidation status of PKM2-M239 functionally regulates PKM2 activity in an MSRA-dependent manner.

PKM2 activation promotes PDA metastasis

PKM2 activators have been shown to suppress primary tumor formation in xenograft models (Anastasiou et al., 2012). Likewise, at a concentration that increases oxidative phosphorylation (Figure S6A), we observed that pharmacological activation of PKM2 by TEPP46 suppresses PDA^{T} cell proliferation (Figure S6B). In addition, however, this treatment also increases the ability of these cells to migrate (Figure 6A) and to accumulate aspartate (Figure S6C). Given that MSRA loss promotes PDA migration through the activation of PKM2 (Figures 5F and S5D), we used two orthogonal approaches to ask whether pharmacological activation of PKM2 can promote cancer metastasis. First, to ascertain if transient activation of PKM2 in established tumors can promote distant metastasis, we implanted luciferase-expressing PDA^{T} cells subcutaneously into the flanks of mice (Figure 6B). When tumors reached 100 mm^3 in volume, the mice were randomly assigned into two treatment cohorts, one administered with vehicle, and the other with TEPP46. After 5 days of treatment the primary tumors were surgically resected, at which time the tumor volumes were similar in both cohorts (Figure 6C). Treatment was withdrawn 2 days after surgery and the cohorts were monitored for an additional month. Although neither cohort developed distant metastasis at the end of one month, we unexpectedly found that the TEPP46-treated group exhibits increased recurrence at the primary tumor site compared to the vehicle group (Figures 6D and S6D). Second, we examined the effect of constitutive PKM2 activation using a liver metastasis model based on intrasplenic injection of luciferase-expressing PDA^{T} cells. In this experiment, mice were randomly enrolled into

vehicle or TEPP46 treatment cohorts after surgery (Figure 6E) and liver colonization was monitored by intravital bioluminescence imaging over a period of three weeks. While we observed no change in body mass between the vehicle and the TEPP46 treatment groups (Figure S6E), the latter exhibited a significant increase in liver colonization (Figures 6F, S6F, and S6G). These observations indicate that pharmacological activation of PKM2 can promote regional recurrence and metastatic spread of pancreatic cancer.

Most cancer cells predominantly express PKM2 over PKM1 (Chaneton and Gottlieb, 2012), a phenomenon that we also observed by immunohistochemical (IHC) staining of normal muscle and pancreatic tumor tissues (Figure S6H). Interestingly, although expression of constitutively active PKM1 is minimal in primary pancreatic tumors, we detected various degrees of PKM1 expression in liver metastases from KPC mice (Figure S6I). Indeed, since PKM1 expression can also give rise to more aggressive disease in a KRAS-G12D-induced model of non-small cell lung cancer (Morita et al., 2018), and genetic replacement of PKM2 with PKM1 in some mouse models has been shown to enhance tumor development (Dayton et al., 2016) and metastasis (Israelsen et al., 2013), the induction of pyruvate kinase activity may represent a general mechanism of metastatic transformation. Whether achieved by the induction of PKM1 expression or through MSRA-dependent oxidation of PKM2-M239, the consequent increase of pyruvate kinase activity would support the bioenergetic and biosynthetic needs of metastasis (Figure 6G).

DISCUSSION

The impact of ROS on cancer is complex, as is evident by their context-dependent ability to either promote (Porporato et al., 2014) or suppress (Piskounova et al., 2015; Wiel et al., 2019) tumorigenesis. Interpreting the effects of ROS on cellular behavior is complicated by their dual potential to indiscriminately oxidize macromolecules or to selectively oxidize redox-reactive residues of target proteins. Indeed, it is well established that the thiol group of proteinaceous cysteines can serve as reversible redox switches that regulate distinct signaling outcomes (Paulsen and Carroll, 2013). In addition to cysteine, methionine residues also harbor a redox-reactive sulfur atom that can be readily oxidized *in vivo*. Here, we report that the methionine sulfoxide reductase MSRA is a potent suppressor of PDA metastasis. Importantly, in this setting, MSRA loss does not perturb global redox homeostasis. Moreover, the ability of MSRA to inhibit cell migration cannot be recapitulated by exogenous antioxidants, suggesting that enzymatic control of site-specific redox signaling is essential for metastasis and further highlighting the functional distinctions between global ROS perturbation and site-specific redox signaling.

To elucidate the mechanisms by which MSRA loss promotes metastatic spread, we surveyed the proteome using chemoproteomic tools and identified the conversion of phosphoenolpyruvate to pyruvate by PKM2 as a key metabolic node regulated by MSRA. The conformation of PKM2 is tightly controlled by allosteric factors that regulate the equilibrium between the less active dimeric state and highly active tetramers, allowing cellular metabolism to shift between glycolysis and mitochondrial respiration, respectively (Christofk et al., 2008b; Hitosugi et al., 2009). Thus, PKM2 oligomerization is a decision point that determines not only the activity of the enzyme, but also whether glucose

metabolism ensues by glycolysis or respiration. Remarkably, we found that oxidation of methionine M239 promotes PKM2 tetramerization and its enzymatic activity in metastatic PDA cells. These data suggest that methionine oxidation can act as a bona fide redox switch, in this case by directing glucose metabolism to either the glycolytic (reduced PKM2-M239) or oxidative (oxidized PKM2-M239) pathway. Interestingly, in contrast to the oxidation of M239, oxidation of the allosteric hub cysteine C358 ablates PKM2 enzymatic function (Anastasiou *et al.*, 2011). Of note, we found that PKM2 methionine oxidation occurs more rapidly than that of cysteine oxidation, consistent with the activating function of M239 oxidation to support metabolic switching and the inactivating function of C358 in response to oxidative stress. These observations not only illustrate how distinct site-specific oxidation events can yield disparate biochemical consequences but also demonstrate that sophisticated sulfur-based redox signaling govern the properties of cancer cells at different stages of tumor development.

Although aerobic glycolysis is a hallmark of proliferating cancer cells (Shaw, 2006), a definitive metabolic pattern that distinguishes metastatic from non-metastatic tumors has not yet been identified (Bergers and Fendt, 2021). Several lines of evidence suggest that mitochondrial respiration is favored by metastatic cancer cells (Caino et al., 2015; Caino et al., 2016; Hooda et al., 2013; Kulawiec et al., 2009; LeBleu et al., 2014; Nie et al., 2020; Rademaker et al., 2019; Rodrigues et al., 2016; Yamaguchi et al., 2019; Zhou et al., 2018). Here, we establish methionine oxidation of PKM2 to be a metabolic switch that promotes this phenotype. Mitochondrial respiration may facilitate metastasis by powering both the biosynthesis of cell components and the bioenergetics of cell migration. For example, complex III promotes the activation of the pyrimidine biosynthetic enzyme DHODH (Fang et al., 2013), which has been shown to support liver metastasis (Yamaguchi *et al.*, 2019). In this study, we observed that exogenous aspartate and asparagine, both products of mitochondrial respiration (Birsoy *et al.*, 2015; Krall *et al.*, 2021; Sullivan *et al.*, 2015), can directly promote cell migration. Although the mechanisms by which these biosynthetic pathways contribute to metastasis remain to be determined, these observations raise the possibility that mitochondrial metabolites may directly elicit changes in the cytoskeleton or cell membrane that support migration and metastasis.

Limitations of the study

To fully exploit the therapeutic potential of our finding, additional work is needed to decipher the post-translational regulators of MSRA and the contexts under which they promote MSRA degradation. Metabolic flux analysis with finer time points to compare the loss of MSRA to MSRB family members should reveal whether stereospecific differences in methionine oxidation influence metabolic functions. Lastly, in this study, reactive methionines were profiled using oxaziridine probes on lysates at the whole-cell level. The development of reagents with improved organelle specificity and cell permeability will enable in-situ characterization of reactive methionines with greater subcellular specificity, resolution, and proteomic coverage.

STAR METHODS

RESOURCE AVAILABILITY

Lead contact—Further information and requests for resources and reagents should be directed to and will be fulfilled by the lead contact Iok In Christine Chio (christine.chio@columbia.edu).

Materials availability—All organoid lines, cell lines, plasmids, and chemical reagents generated can be obtained via a UCB or CUIMC materials transfer agreement (free of charge for non-commercial purposes).

Data and code availability

- The proteomics and metabolomics data have been deposited in the MassIVE. Accession numbers are listed in the key resources table. The mass spec datasets generated for these studies are also available as supplemental data provided with this manuscript.
- This paper does not report original code.
- Any additional information required to reanalyze the data reported in this paper is available from the lead contact upon request.

EXPERIMENTAL MODEL AND SUBJECT DETAILS

Mouse Models—*Trp53*$^{+/LSL\text{-}R172H}$, *Kras*$^{+/LSL\text{-}G12D}$, *Pdx1-Cre,* strains in C57Bl/6J background were interbred to obtain *Pdx1-Cre; Kras*$^{+/LSL\text{-}G12D}$*; Trp53*$^{+/LSL\text{-}R172H}$ (KPC) (Hingorani *et al.*, 2005) mice for organoid isolation. C57Bl/6J mice were purchased from the Jackson Laboratory for the isolation of N organoids and for syngeneic orthotopic or intrasplenic transplant experiments. All animal experiments were conducted in accordance with procedures approved by the IACUC at Columbia University (AC-AABK554). All transplants were performed in 8-week-old gender balanced cohorts of C57Bl/6J mice and analyzed accordingly to the timeline described in the Results section and below:

Orthotopic engraftment in the pancreas: Orthotopic engraftment of mouse pancreatic organoids was conducted as described (Boj *et al.*, 2015). In brief, mice were anesthetized using isoflurane, and Carprofen (5 mg kg^{-1}), which was subcutaneously administered. 10^5 cells were transplanted to the parenchyma of the pancreas. The abdominal wall was sutured with absorbable vicryl sutures (Ethicon Cat# J392H), and the skin was closed with wound clips (CellPoint Scientific Inc. Cat# 203-1000). Allograft-bearing mice were subjected to high-contrast ultrasound imaging using the Vevo 2100 System with a MS250, 13–24 MHz scanhead (Visual Sonics, Inc, Amsterdam, NL) to monitor tumor kinetics intravitally. To induce expression of MSRA, doxycycline was administered to mice through daily oral gavage.

Intrasplenic injection: Mice were anesthetized using isoflurane, and Carprofen (5 mg kg^{-1}), which was subcutaneously administered. Tumor cells (10^5 cells) were injected into the spleen of gender matched 8-week-old C57Bl/6J mice. The spleen was resected 3 minutes

later applying ligation clips (Horizon Titanium Ligating Clips Teleflex #002200). The abdominal wall was sutured with absorbable vicryl sutures (Ethicon Cat# J392H), and the skin was closed with wound clips (CellPoint Scientific Inc. Cat# 203-1000). To induce expression of MSRA, doxycycline was administered to mice through daily oral gavage.

***In vivo* assessment of PKM2 activation on metastasis:** Subcutaneous injection model: One million luciferase-expressing PDA^T cells were injected subcutaneously into the flanks of mice. 12 days after transplantation, animals were randomly assigned to the vehicle control group (0.5% carboxymethylcellulose, 0.1% Tween80 in ddH_2O) or TEPP46 treatment group (50 mg kg^{-1}). Animals were dosed twice a day by oral gavage for 7 days. Tumor volume was monitored by caliper measurements using the following formula: tumor volume [mm^3] = (length [mm]) × (width [mm]) × (height [mm]) × (π/6). To monitor for potential metastasis, mice were subject to bioluminescent imaging using the IVIS spectrum (PerkinElmer Cat# 124262) after injection with 150 mg kg^{-1} D-Luciferin (Goldbio Cat# LUCK).

Intrasplenic injection model: 50,000 luciferase-expressing PDA^T cells were injected into the spleen as described above, after which animals were randomly assigned to the vehicle control group (0.5% carboxymethylcellulose, 0.1% Tween80 in ddH_2O) or TEPP46 treatment group (50 mg kg^{-1}). Animals were dosed twice a day by oral gavage. Body weight and tumor burden were measured at enrollment and once a week throughout the course of the study. To monitor tumor burden in the liver, mice were subject to bioluminescent imaging using the IVIS spectrum (PerkinElmer Cat# 124262) after injection with 150 mg kg^{-1} D-Luciferin (Goldbio Cat# LUCK).

Human Specimens

Rapid Autopsy Samples: Human pancreatic tumor and liver metastatic specimens from decedents who have previously been diagnosed with pancreatic ductal adenocarcinoma were obtained from the University of Nebraska Medical Centre's Rapid Autopsy Program (RAP) for Pancreas in compliance with IRB 091-01 (Table S1). To ensure specimen quality, organs were harvested within three hours post-mortem and the specimens flash frozen in liquid nitrogen or placed in formalin for immediate fixation. Sections are cut from paraffin blocks of formalin fixed tissue into 4 μm thick sections and mounted on charged slides.

Columbia Tissue Bank resected samples: Deidentified Human pancreatic tumor and adjacent normal specimens from patients diagnosed with pancreatic ductal adenocarcinoma were obtained from the Herbert Irving Comprehensive Cancer Centre (HICCC) Tissue Bank through surgical resections in compliance with IRB AAAR7565 (Table S1). Tissue Microarray: 23 adjacent normal pancreatic tissues and 23 PDA tissues, 5 μm thickness of sections, size of each tissue core punched: 2.0 mm.

Cell Culture Models

Organoid isolation and culture: Detailed procedures to isolate and propagate murine and human, normal and neoplastic pancreatic organoids have been described previously (Boj *et al.*, 2015; Huch et al., 2013). In brief, organoids were maintained in complete organoid

media: Advanced DMEM/F12 (Gibco Cat#12634010) supplemented with 1% Penicillin/Streptomycin (PS) (Gibco Cat# 15140163), 1× GlutaMAX (Gibco Cat# 35050061), 1× HEPES (Gibco Cat# 15630080), 1× B27 (Invitrogen Cat# 17504044), 1.25 mM N-Acetylcysteine (NAC) (Sigma-Aldrich Cat# A9165), 10 nM gastrin (Sigma-Aldrich Cat# G9145), 50 ng ml^{-1} EGF (PeproTech Cat# 315-09), 10% RSPO1-conditioned media, 20% Noggin-FC-conditioned media (the Noggin-Fc-expressing cell line was a kind gift from Dr. Gijs R. van den Brink, University of Amsterdam), 100 ng ml^{-1} FGF10 (PeproTech Cat# 100-26), and 10 mM Nicotinamide (Sigma-Aldrich Cat# N0636). To passage, organoids were washed out from the GFR-Matrigel (Corning Cat# 356231) using cold Advanced DMEM/F12 supplemented 1% PS, 1× GlutaMAX and 1× HEPES, and mechanically dissociated into small fragments using fire-polished glass pipettes, and then seeded into fresh GFR-Matrigel. Passaging was performed at a 1:4 split ratio roughly twice per week. All experiments described were done in the absence of EGF and NAC (Chio *et al.*, 2016). To isolate p53 LOH (loss of heterozygosity) organoids, early-passage tumor (*Pdx1-Cre; Kras*$^{+/LSL\text{-}G12D}$*; Trp53*$^{+/LSL\text{-}R172H}$) organoids were cultured in complete organoid media with 10 μM Nutlin-3a (Sigma-Aldrich Cat# SML0580-5MG;) and propagated for three passages. p53 LOH was confirmed by PCR (Hingorani *et al.*, 2005) using the following primers: p53 loxP Fw: 5'AGCCTGCCTAGCTTCCTCAGG and p53 loxP Rv: 5'CTTGGAGACATAGCCACACTG.

Monolayer cultures: Monolayer KPC primary pancreatic cancer cells were generated from tumors derived from KPC mice. HEK293T cell line was from ATCC (Cat# CRL-3216). All cells were cultured in DMEM (Gibco Cat#11995073) supplemented with 10% fetal bovine serum (FBS) (Corning Cat# 35-010-cv) and 1% PS unless stated otherwise. All cells were cultured at 37 °C with 5% CO_2.

METHOD DETAILS

CRISPR/Cas9-mediated gene deletion—Pancreatic cancer cells and organoid lines were transduced with lentivirus expressing Cas9 (EFS-Cas9-P2A-Puro, Addgene # 108100). In this study, all sgRNAs targeting mouse genes were cloned into LRC2.1T (U6-sgRNA-Cherry, Addgene # 108099). Single sgRNAs were cloned by annealing two DNA oligos and T4 DNA ligation into a BsmB1-digested LRC2.1T as described (Shi et al., 2015). The design principle of sgRNA was based on previous reports: (1) sgRNAs with the predicted low off-target effect (Hsu et al., 2013) and (2) sgRNAs targeting the functional protein domain region (Shi *et al.*, 2015), for which sequence information was retrieved from NCBI Conserved Domains Database. To improve U6 promoter transcription efficiency, an additional 5' G nucleotide was added to all sgRNA oligo designs that did not already start with a 5' G. gRNA sequences used to target MSRA are: CACCGTACACAACCCGGACGACTT (sg*MsrA*9.1), and AAACCCGTGCAGATGGAAGCAGCC (sg*MsrA*10.1). gRNA sequence against the ROSA locus was used as a negative control: GAAGATGGGCGGGAGTCTTC.

Lentiviral and retroviral production and infection—pLenti-Cas9, LRC2.1T-sgRNA, pLKO.1 lentiviruses were produced in HEK293T cells co-expressing the packaging vectors (pPAX2, Addgene # 12260 and VSVG, Addgene # 12259), concentrated with LentiX

concentrator (Clontech Cat# 631232), and resuspended with DMEM supplemented with 10% FBS and 1% PS at 5× concentration or Advanced DMEM/F12 (Gibco Cat#12634010) supplemented with 1% PS, 1× GlutaMAX (Gibco Cat# 35050061), and 1× HEPES (Gibco Cat# 15630080) at 10× concentration. Mouse pBabe (Addgene # 1764 and # 1767), MSCV-luciferase (Addgene # 18782) retroviruses were produced in Phoenix-ECO cells (ATCC Cat# CRL-3214), concentrated with RetroX Concentrator (Clontech Cat# 631456), and resuspended in DMEM supplemented with 10% FBS and 1% PS at 5× concentration, or Advanced DMEM/F12 (Gibco Cat#12634010) supplemented with 1% PS, 1× GlutaMAX (Gibco Cat# 35050061), and 1× HEPES (Gibco Cat# 15630080) at 10× concentration. Two hundred thousand cells were plated and infected with 5× concentrated virus with 5 μg ml^{-1} polybrene (Millipore Sigma Cat# TR1003G) and spinoculated at 600 g for 45 min at room temperature. For organoids, spinoculated cells were kept at 37 °C with 5% CO_2 for 6 h prior to replating in Matrigel and organoid media. One day after infection, pLenti-Cas9, pBabe, or MSCV-luciferase infected cells were treated with 2 μg ml^{-1} puromycin (Sigma-Aldrich Cat # P9620), 1 mg ml^{-1} neomycin (Research Products International Cat# G64500-10.0) or 500 μg ml^{-1} hygromycin (Fisher Scientific Cat# 10687010) for selection.

Cell proliferation assay—Cell proliferation assay was performed by seeding 3,000 pancreatic cancer cells per well in optical bottom, black 96-well plates (Corning Cat# 3603) or opaque 96-well plates (Corning Cat# 3917). Cells were seeded in Gibco Fluorobrite DMEM (ThermoFisher Cat# A1896701) supplemented with 10% FBS, 1% PS and 1% GlutaMAX (ThermoFisher Cat# 35050061). Cell viability was measured every 24 hours by area covered using CellInsight CX7 or using a luminescent ATP-based assay (CellTiter-Glo, Promega Cat# G7573) with a plate reader (SpectraMax i3x, Molecular Devices). Data were analyzed with GraphPad Prism.

Cell invasion assay—Cell invasion was measured using the CHEMICON Cell Invasion Assay Kit (Sigma-Aldrich Cat# ECM550) based on the manufacturer's instructions. In brief, cells were starved in HBSS (Gibco Cat# 14025092) for 24 hours prior to seeding. 50,000 cells were seeded per invasion chamber in serum free Gibco Fluorobrite DMEM (ThermoFisher Cat# A1896701) supplemented with 1% PS and 1% GlutaMAX (ThermoFisher Cat# 35050061). Each invasion chamber contains an 8 mm por size polycarbonate membrane, over which a thin layer of ECMatrixTM is dried. The lower chamber contains Fluorobrite DMEM (ThermoFisher Cat# A1896701) supplemented with 10% FBS, 1% PS and 1% GlutaMAX (ThermoFisher Cat# 35050061). Cells that have migrated through the polycarbonate membrane are incubated with Cell Stain Solution, then subsequently extracted, and detected on a standard microplate reader (560 nm).

Cell migration assay—Cell migration assay was performed by seeding 15,000 pancreatic cancer cells per well in optical bottom, black 96-well plates (Corning Cat# 3603). Cells were seeded in Gibco Fluorobrite DMEM (ThermoFisher Cat# A1896701) supplemented with 10% FBS, 1% PS and 1% GlutaMAX (ThermoFisher Cat# 35050061). Cells were incubated for 48 hours to form fully confluent monolayer before proceeding to the wound making step. A scratch was made at the center of each well using the BioTek AutoScratchTM Wound Making Tool, and wells were washed with PBS to remove debris. Following the wash step,

imaging media (Fluorbrite DMEM, 1% FBS, 1% GlutaMAX, 1% PS) were added and wells were imaged every 6 hours using the BioTek Cytation 5 automated live-cell fluorescence imaging system in conjunction with the BioSpa Automated Incubator (BioTek Instruments, INC) to monitor wound closure. Environmental conditions were maintained at 5% CO_2 and 37 °C throughout the imaging period.

Reactive methionine profiling

Sample preparation: Organoid lysates at 1 mg ml^{-1} in RIPA buffer (50 mM Tris pH 7.4, 0.5% Deoxycholate, 0.1% SDS, 150 mM NaCl, 2 mM EDTA, 1% NP40) were labelled with 200 μM Oxaziridine-alkyne probe at room temperature for 40 min and quenched by acetyl-methionine. The CuAAC reactions were performed on the labelled protein using 200 μM photo-cleavable biotin azide probe (Click Chemistry Tools Cat# 1119). Samples were precipitated and washed with cold acetone and dissolved in 2% SDS/TEAB. The solutions were diluted to 0.1% SDS/TEAB and then added with streptavidin agarose beads overnight at 4 °C with agitation. The agarose beads were washed twice with 1% Triton X-100/TEAB and twice with TEAB. The washed beads were then reduced with 5 mM TCEP at 65 °C for 15 min and alkylated with 10 mM iodoacetamide at 37 °C for 30 min. On-beads trypsin/lysC (1:50) digestion were performed at 37 °C for 16 h. After washing twice with TEAB, the beads were subjected to UV irradiation for 40 min. The eluents were collected and quantified using peptide fluorescent quantification kit (Thermo Scientific Cat# 23290). Same amounts of peptides from each sample were labelled with a channel of TMT 10plex following the manufacturer's protocol and combined together. TMT labelled peptides were dried using lyophilizer.

LC-MS/MS analysis: LC separation was done on a Dionex nano Ultimate 3000 (Thermo Scientific) with a Thermo Easy-Spray source. The digested peptides were reconstituted in 2% acetonitrile/0.1% trifluoroacetic acid and 1 μg in 5 μl of each sample was loaded onto a PepMap 100 Å 3U 75 um × 20 mm reverse phase trap where they were desalted online before being separated on a 100 Å 2U 50 micron × 150 mm PepMap EasySpray reverse phase column. Peptides were eluted using a 120 minutes gradient of 0.1% formic acid (A) and 80% acetonitrile (B) with a flow rate of 200 nl min^{-1}. The separation gradient was run with 2% to 5% B over 1minute, 5% to 50% B over 89 minutes, 50% to 99% B over for 2 minutes, a 4-minutes hold at 99% B, and finally 99% B to 2% B held at 2% B for 18 minutes.

MS3 Synchronous Precursor Selection Workflow: Mass spectra were collected on a Fusion Lumos mass spectrometer (ThermoFisher Scientific) in a datadependent MS3 synchronous precursor selection (SPS) method. MS1 spectra were acquired in the Orbitrap, 120K resolution, 50 ms max inject time, 5×10^5 max inject time. MS2 spectra were acquired in the linear ion trap with a 0.7 Da isolation window, CID fragmentation energy of 35%, turbo scan speed, 50 ms max inject time, 1×10^4 AGC and maximum parallelizable time turned on. MS2 ions were isolated in the iontrap and fragmented with an HCD energy of 65%. MS3 spectra were acquired in the orbitrap with a resolution of 50K and a scan range of 100–500 Da, 10^5 ms max inject time and 1×10^5 AGC.

Methionine proteome identification and quantification: The Thermo binary instrument files were processed with MSConvert from the Proteowizard toolkit (Chambers et al., 2012) and Python scripts from the PAW (Proteomic Analysis Workflow) pipeline https://github.com/pwilmart/PAW_pipeline (Wilmarth et al., 2009) to create MS2-format files (McDonald et al., 2004) for database searching and to extract the reported ion peak heights from individual MS3 scans. Database searching used Comet version 2016.01 rev. 3 (Eng et al., 2013) with the PAW pipeline for peptide spectrum match (PSM) validation using the target/decoy method (Elias and Gygi, 2007). Search parameters included: parent ion monoisotopic mass tolerance 1.25 Da, fragment ion monoisotopic mass tolerance 1.0005 Da, trypsin cleavage with up to two missed cleavages, variable oxidation and oxaziridine labeling of Met residues, fixed alkylation of Cys residues, and fixed TMT reagent masses (+229.1620 Da) at peptide N-terminus and Lys residues. The protein database of *Mus musculus* (UP000006540) was used to map the identified peptides. Common contaminants (179 sequences) and sequence-reversed decoys were also appended. Peptide-spectrum matches were filtered to a 1% false discovery rate (FDR) and mapped to proteins using basic parsimony rules. Protein identifications required at least two distinct PSMs per protein per TMT plex. An additional extended parsimony protein grouping step was used to combine highly homologous proteins into the final list of identified proteins. Shared or unique peptide status was defined in the context of the final protein list (Table S2). Reporter ion intensities from PSMs associated with unique peptides were summed into protein total intensity values. Protein intensities within each TMT plex and between plexes were normalized using the Internal Reference Scaling (IRS) method https://github.com/pwilmart/IRS_normalization (Plubell et al., 2017) on the average of two reference pools generated from pooling all samples in the experiment.

Data statistics analysis: For differential comparison of proteomics data, the limma package was used (Smyth, 2004). A p value < 0.05 and q value < 0.1, determined by limma, was used to identify differentially oxidized proteins. Only unique peptides that were identified/quantified in at least two samples were listed in Tables S3 and S4 and used for fold change calculation.

KEGG pathway analysis: For each protein that was assigned as differentially oxidized by the above statistics analysis, UniProt accession number was converted to KEGG gene ID using the online ‘Convert ID’ tool https://www.genome.jp/kegg/mapper/convert_id.html. The protein IDs were then submitted to https://www.genome.jp/kegg/pathway.html for pathway analysis.

Metabolomics

Cell treatment and harvest: All LC-MS grade solvents and salts were purchased from Fisher: water, acetonitrile, methanol, formic acid, ammonium acetate and ammonium formate. The authentic metabolite standards and N-ethylmaleimide were purchased from Sigma-Aldrich. One million pancreatic cancer cells were grown in DMEM (Gibco Cat#A1443001) supplemented with 10% dialyzed FBS (Gibco Cat# 26400044), 2 mM Glutamine, and 1% PS. For tracing experiments, $^{13}C_6$-Glucose (17.5 mM)-containing media were used to replace ^{12}C media for 30 minutes. ^{12}C-Tracer control samples were subject

to the same treatment except ^{12}C-media were used for replacement. These samples validate that ^{13}C -incorporation is not an interfering ion. Cells were washed in cold 150 mM ammonium formate (pH 7.4) containing 1 mg ml^{-1} N-ethylmaliemide to protect free thiols and quenched in cold (−30 °C) 50% methanol (v/v) containing 1 mg ml^{-1} N-ethylmaleimide at a volume of 230 µl. Cells were scraped and transferred to a pre-chilled 2 ml Eppendorf brand tube containing 6 washed ceramic beads inside (1.4 mm). Another 150 µl of the methanol mixture was added to the dish and scraping was repeated and transferred to the tube. A 220 µl volume of −30 °C cold acetonitrile was added to each sample followed by vortexing. Samples were then subject to 2 minutes of bead beating at 30 Hz (Qiagen tissue lyser, Retsch). Dicholoromethane (600 µl) and ice-cold water (300 µl) were added and samples were vortexed. Samples were allowed to partition on ice for 10 min and centrifuged for 10 min at 4,000 rpm (1503 g) with temperature maintained at 1 °C (Eppendorf 5424 R). The aqueous supernatants were dried by vacuum centrifugation with sample temperature maintained at −4 °C (Labconco, Kansas City MO, USA). At time of analysis, dried extracts were subsequently re-suspended in 30 µl of chilled H_2O and clarified by centrifugation for 5 min at 15000 rpm (21130g) at 1 °C. Sample injection volumes for UPLC-QTOF tracer analyses were 5 µl per injection.

UPLC-QTOF Tracer analysis: Samples were injected onto an Agilent 1290 Infinity II UHPLC system which was connected to an Agilent 6530 quadrupole time-of-flight mass spectrometer (UPLC-QTOF-MS). Eluent ionization was achieved using Dual Agilent Jet Stream electrospray ionization source in negative mode. The source-gas temperature and flow were set at 300 °C and 8 l min^{-1}, respectively. The nebulizer pressure was set at 35 psi. The capillary voltage was set at 3500 V and the nozzle voltage was set to 1000 V. The sheath gas temperature and flow rate were set to 350 °C and 11 l min^{-1}, respectively. A reference spray was infused continuously for constant internal mass calibration. The m/z of the two ions monitored were 119.0363 (purine) and 980.1638 (HP-0921 acetate adducts) with a detection window of 20 ppm and a minimum height of 1000 counts. The mass range monitored was from 75 to 2000 m/z with an acquisition rate of 1 spectra/s. Data were stored in both centroid and profile formats.

Metabolite separation was achieved by using a Zorbax Extend C18 column 1.8 µm, 2.1 × 150 mm^2 with guard column 1.8 µm, 2.1 × 5 mm^2 (Agilent Technologies). The chromatographic gradient started at 100% mobile phase A (97% water, 3% methanol, 10 mM tributylamine, 15 mM acetic acid, 5 µM medronic acid) for 2.5 min, followed with a 5-min gradient to 20% mobile phase B (methanol, 10 mM tributylamine, 15 mM acetic acid, 5 µM medronic acid), a 5.5-min gradient to 45% B and a 7-min gradient to 99% B at a flow rate of 0.25 ml min^{-1}. This was followed by a 4-min hold time at 99% mobile phase B. The column was restored by back-washing with 100% mobile phase C (90% acetonitrile) by using a 1260 isocratic pump for 3 min which ramps from 0.25 ml min^{-1} to 0.600 ml min^{-1} after which it is held for 0.25 min. The column was then re-equilibrated at 100% A over 7.65 min at a forward flow rate of 0.400 ml min^{-1}. The flow was brought back to 0.25 ml min^{-1} for the next injection. The column temperature was maintained at 35 °C. Retention times and MS/MS (unlabeled Tracer control samples) were compared to 269 metabolites (207 in standard mix, 34 validated (not in standard mix), and 28 compounds from the Agilent Ion

pairing library, not fully validated by the facility). All compounds reported in this article have been validated. Data analysis and mass isotopologue extraction were carried out using ProFinder software version 10.0.2, Build 10.0.2.162 (Agilent Technologies).

GC-MS Stable Isotope Tracer analysis: After LC-QTOF analysis 30 µl of each remaining sample was transferred to a glass GC-MS vial insert to which 1 µl of 750 ng ml^{-1} D_{27}-Myristic acid standard was added. The samples were then dried by vacuum centrifugation at −4 °C (Labconco). In order to protect and stabilize α-keto acids (pyruvate, α-ketoglutarate etc.), dried sample pellets were resuspended in 30 µl pyridine containing 10 mg ml^{-1} methoxyamine hydrochloride (Sigma-Aldrich Cat# 226904), vortexed, and sonicated to ensure dissolution. Following 30 min of incubation at room temperature, samples were transferred to sealed autoinjection vials containing 70 µl of *N-tert*-Butyldimethylsilyl-*N*-methyltrifluoroacetamide (MTBSTFA) (Sigma Cat# M-108). Vials were incubated for 1 h at 70 °C.

Derivatized samples were subjected to GC-MS analysis using an Agilent 5975C GC-MS equipped with a DB-5MS+DG (30 m × 250 µm × 0.25 µm) capillary column (Agilent J&W). All samples were injected three times: twice using scan (50–700 m/z) mode (1× and 6× dilution) and once using selected ion monitoring (SIM) mode. 1 µl of the derivatized sample was injected in the GC in splitless mode with inlet temperature set to 280 °C and electron impact set at 70 eV. Helium was used as the carrier gas with a flow rate such that myristic acid eluted at approximately 18 min. The quadrupole was set at 150 °C and the GC-MS interface at 285 °C. The oven program started at 60 °C held for 1 min, then increasing at a rate of 10 °C min^{-1} until 320 °C. Bake-out was at 320 °C for 10 min. All metabolites used in this study were previously validated using authentic standards to confirm mass spectra and retention times. Integration of ion intensities (generally M-57 ion) was done using the Agilent MassHunter Quant software (Agilent Technologies). Mass isotopologue distribution analysis was carried out using an in-house algorithm adapted from (Nanchen et al., 2007).

Extracellular acidification rates measurement (ECAR)—Ten thousand cells were plated as organoids in 2 µl Matrigel domes or directly in monolayer in XF96 cell culture microplates (Seahorse Biosciences Cat#101104-004) in EGF and NAC-free organoid complete media (for organoids) or Flurobrite DMEM supplemented with 10% FBS (for monolayer cells). After 24 h, growth media were changed to bicarbonate-free assay media (XF assay medium, Seahorse Biosciences, Cat# 102365-100) and incubated at 37 °C for 1 h in a CO_2-free incubator. Extracellular acidification rate (ECAR) was measured using an XF96 Extracellular Flux Analyzer (Seahorse Biosciences) under basal conditions and following addition of glucose (10 mM), Oligomycin (1 µM), and the glucose analogue, 2-deoxyglucose, 2DG (50 mM), according to the manufacturer's protocol.

Oxygen consumption rates measurement (OCR)—Ten thousand cells were plated as organoids in 2 µl Matrigel domes or directly in monolayer in XF96 cell culture microplates (Seahorse Biosciences Cat# 101104-004) in EGF and NAC-free organoid complete media (for organoids) or Fluorobrite DMEM supplemented with 10% dialyzed FBS (for monolayer cells). After 24 h, growth media were changed to bicarbonate-free

assay media (XF assay medium, Seahorse Biosciences, Cat# 102365-100) and incubated at 37 °C for 1 h in a CO_2-free incubator. Oxygen consumption rate (OCR) was measured using an XF96 Extracellular Flux Analyzer (Seahorse Biosciences) under basal conditions or following the addition of Oligomycin (1 μM), the uncoupler FCCP (0.5 μM), and the electron transport inhibitor Rotenone/Antimycin A (0.5 μM), according to the manufacturer's protocol.

Immunoprecipitations—Cells were lysed with Flag IP lysis buffer (50 mM Tris-HCl, 150 mM NaCl, pH 7.4, 1 mM EDTA, 1% TRITON X-100) on ice and cleared by centrifugation at 16, 000 g for 10 min. Anti-Flag M2 magnetic beads were washed three times with TBS buffer (50 mM Tris-HCl, 150 mM NaCl, pH 7.4) and then incubated for 1 h with soluble lysates. Beads were washed four times with TBS buffer and eluted with 3× Flag peptide (200 ng μl^{-1}).

PKM2 oligomerization assay

Endogenous PKM2: Cells were lysed with native lysis buffer (Abcam Cat# ab156035) on ice and cleared by centrifugation at 16, 000 g for 10 min. Clear lysates were added 0.025% glutaraldehyde (Alfa Aesar Cat# A10500) and incubated at 37 °C for 3 min. Reaction was quenched with 1M Tris-HCl, pH 7.5 (Invitrogen Cat# 15567027). Samples were added NuPAGE LDS sample buffer (Invitrogen Cat# NP0007) and separated by NuPAGE 3–8% Tris-Acetate gel (Invitrogen Cat# EA0375BOX), and subject to immunoblotting analysis.

PKM2 immunoprecipitated from cells: For PKM2-Flag immunoprecipitated from HEK293T cells or PDA^T cells, protein was eluted with 3× Flag peptide (200 ng μl^{-1}) in HEPES buffer (25 mM HEPES, 150 mM NaCl, pH 7.4) and the concentration was determined by BCA (Thermo Scientific Cat# 23227). 5 μM protein was subject to glutaraldehyde (0.025%) crosslinking. After quenching with 1M Tris-HCl (Invitrogen Cat# 15567027), samples were loaded to 4–12% Bis-Tris gel (GenScript Cat# M00654) and subject to immunoblotting analysis.

Size exclusion chromatography: Cells were lysed with native lysis buffer (Abcam Cat# ab156035) on ice and cleared by centrifugation at 16, 000 g for 10 min. ~ 1 mg of cellular protein was separated on a Enrich SEC 650 10 × 300 column (Bio-Rad) in PBS buffer (50 mM sodium phosphate, 150 mM NaCl, pH 7.2). Fractions were concentrated using Amicon Ultra-0.5 ml Centrifugal Filters (Millipore Cat# UFC501024) and subject to immunoblotting analysis.

Pyruvate kinase activity assay—*In vitro* measurement of pyruvate kinase activity on proteins immunoprecipitated from HEK293T or murine pancreatic cancer cells was conducted as in(Chaneton et al., 2012). Briefly, PKM1 (4 nM) or PKM2 (200 nM) were incubated in the reaction buffer (50 mM Tris, pH 7.5, 100 mM KCl, 100 mM $MgCl_2$, 200 μM PEP, 200 μM ADP) for 20 min on a shaker before addition of equal volume of Kinase-Glo Plus reagent (Promega Cat# V3771), as per the manufacturer's instructions. Luminescence was read with Synergy™ Mx Microplate Reader (BioTek). *In vitro* measurement of pyruvate kinase activity in the murine pancreatic cancer cell lysates

was carried out using pyruvate kinase activity assay kit (Sigma-Aldrich Cat# MAK072) and the fluorometric assay was conducted following the manufacturer's protocol. To measure PKM2 activity on endogenous PKM2 immunoprecipitated from paired PDA^T and PDA^M cells, cells were lysed with pyruvate kinase activity assay buffer, and 20 μl of immobilized PKM2 antibody (Cell Signaling Technology Cat#13266) was added to 400 μl cleared cell lysate (2 mg cellular protein) and incubated overnight at 4 °C with agitation. Following 3 times wash with kinase activity assay buffer, 5 μl beads were used for activity analysis using pyruvate kinase activity assay kit (Sigma-Aldrich Cat# MAK072) and the fluorometric assay was conducted following the manufacturer's protocol. 10 μl beads were suspended with 15 μl 4× NuPAGE LDS sample buffer (Invitrogen Cat# NP0007) and subject to immunoblotting analysis.

Oxaziridine-alkyne/Iodoacetamide-alkyne/DYn-2/dimedone labeling on PKM— Oxaziridine-alkyne (100 μM), iodoacetamide-alkyne (100 μM) or DYn-2 (5 mM) labeling were conducted on freshly prepared cell lysates or mouse tumor lysates. For endogenous protein, CuAAC reactions were performed using 200 μM desthiobiotin azide probe (Click Chemistry Tools Cat# 1107), followed by acetone precipitation at −20 °C overnight. Acetone was removed by centrifugation and samples were dissolved in 2% SDS/PBS and diluted to 0.1% SDS/PBS. The solutions were added to streptavidin agarose gel (Thermo Scientific Cat# 20353) and incubated at room temperature for 1 h with agitation. After washing with PBS for three times, proteins were eluted from streptavidin agarose gel by adding 4× LDS sample buffer (Invitrogen Cat# NP0007) and boiled at 95 °C for 5 min and blotted for PKM or PKM2. For ectopically expressed PKM2 in HEK293T cells, after labeling with indicated probe, anti-Flag M2 magnetic beads were used for immunoprecipitation. PKM2 proteins were eluted using 3× Flag peptide and labeled with desthiobiotin mediated by CuAAC reaction. The biotinylated level was analysed by immunoblotting using streptavidin-HRP conjugated antibody. For dimedone labeling conducted on ectopically expressed PKM2 in HEK293T cells, 5 mM dimedone (Sigma-Aldrich Cat# D153303) was added into freshly made cell lysate and anti-Flag immunoprecipitation was conducted. After elution, protein was immunoblotted for dimedone-tagged cysteine sulfenic acid (Millipore Cat# 07-2139-I-25UL).

For oxaziridine-alkyne labeled PKM analyzed by quantitative mass spectrometry, on-beads digestion using trypsin/LysC mixture was conducted after probe labeling, biotin installation and streptavidin beads pulldown. Digested peptides were quantified using peptide fluorescent quantification kit (Thermo Scientific Cat# 23290), and same amounts of peptides from each sample were labelled with a channel of TMT 10plex following the manufacturer's protocol and combined for LC-MS/MS analysis. MSFragger (Kong et al., 2017) was used for protein identification and quantification.

$NADP^+$/NADPH and aspartate measurement—The $NADP^+$/NADPH assay was carried out using the NADP/NADPH Assay Kit (BioVision Cat# K347). 2×10^6 murine pancreatic cancer cells were lysed in 400 μl extraction buffer. Lysates were clarified by centrifugation and proteins in the supernatant were removed using Amicon Ultra-0.5 ml Centrifugal Filters (Millipore Cat# UFC501024). The filtrate was used for assays following

the manufacturer's protocol. Total aspartate in murine pancreatic cancer cells was measured using Aspartate Colorimetric/Fluorometric Assay Kit (BioVision Cat# K552). 10^6 cells were lysed in Aspartate Assay Buffer and fluorometric assay was conducted following the manufacturer's protocol. Aspartate amount was normalized to protein amount which is measured using BCA Protein Assay kit (Thermo Scientific Cat# 23227).

Immunohistochemistry and histological assessment—Tissues were fixed in 10% neutral buffered formalin and embedded in paraffin. Sections were subjected to Hematoxylin and Eosin (H&E) staining as well as immunohistochemical staining. Antigen retrieval was done in 10 mM citrate buffer (pH 6). The following primary antibodies were used for immunohistochemical staining at the indicated dilution: MSRA (RRID:AB_2682032, 1:400); MSRB2 (RRID:AB_2813685, 1:100); MSRB1 (RRID: AB_2285669, 1:200); FLAG-M2 antibody (RRID:AB_262044); PKM1(RRID:AB_2715534); PKM2(RRID:AB_1904096). MSRA expression was quantified based on the proportion of positive neoplastic, or normal, ductal epithelial cells. For quantification, the Aperio Cytoplasm Analysis algorithm was used. This algorithm detects the staining intensity of the cytoplasm stained with a specific chromagen (brown). The default values for nuclear staining (hematoxylin) and cytoplasmic staining (brown) were used. The thresholds were set by the veterinary pathologist (J.E.W.) based on the most intense staining in the slide and the lowest intensity deemed positive. Each microarray was evaluated blindly 3 times on 3 different days. Any discrepancies were resolved by re-examination of the disputed spots. Tumors were classified by the veterinary pathologist using standard criteria.

Flow cytometry

Mitochondrial numbers: Cells were labeled in Flurobrite DMEM (for 2D cells) or phenol-red-free Advanced DMEM/F12 media (for organoids) containing 100 nM Mito-tracker Green FM (Cell Signaling Technology Cat# 9074) for 30 min, and analyzed by flow cytometry.

Endogenous ROS level detection: Chemical probe based: Intracellular H_2O_2 level was measured as in (Iwashita et al., 2021). Briefly, murine PDA^T-sgRosa26 or PDA^T-sgMsrA cells were plated on 6-well plates and cultured overnight. Cells were then washed with PBS and incubated with PG1-FM (5 μM) or vehicle (DMSO) in HBSS (Gibco Cat# 14025092) for 30 min. Cells were harvested by 0.05% Trypsin with EDTA (Gibco Cat# 25300054), filtered and analyzed by flow cytometry.

roGFP biosensor based: Subcellular H_2O_2 and GSH redox potential was monitored using roGFP2 biosensors. Briefly, cells were transiently transfected with roGFP2 using jetOPTIMUS (Polyplus Cat# 101000025). Redox status was evaluated using the Attune flow cytometer, with 405, 488 and 531 nm lasers (BD Biosciences, San Jose, CA) and the flow cytometry data was analyzed using the FlowJo software (BD Biosciences). Voltage settings for the SSC, FSC, 405 nm and GFP channels were kept constant for all experiments. Measurements were taken at 405 and 488 nm for calculations of redox ratio. Each analyzed population had a sample size of 10,000 transfected cells.

Western blot analysis—Standard techniques were employed for immunoblotting of organoids. Organoids were harvested using cold PBS on ice. Matrigel was removed with 3 cold PBS washes. Protein lysates were prepared using 0.1% SDS lysis buffer in 50 mM Tris pH 8, 0.5% Deoxycholate, 150 mM NaCl, 2 mM EDTA, 1% NP40, with 1 tablet of PhosSTOP (Roche Cat# 4906837001) and 1 tablet of cOmplete™, Mini, EDTA-free Protease Inhibitor Cocktail (Roche Cat# 11836170001) per 10 ml buffer, and separated on 4–12% Bis-Tris NuPAGE gels (Invitrogen Cat# NP0335BOX) or 12% Bis-Tris SurePAGE Gel (Genscript Cat# M00669; M00667) or 3–8% Tris-Acetate NuPAGE gels (Invitrogen Cat# EA0378BOX), transferred onto a PVDF membrane (Millipore Cat# IPVH00010) and incubated with the indicated antibodies for immunoblotting.

Cytosolic, mitochondrial, and nuclear fractionation of 10^6 PDA^T cells was performed using a Cell Fractionation Kit-Standard (Abcam Cat# ab109719) according to the manufacturer's instructions. Protein abundance in each fraction was analyzed by immunoblotting.

QUANTIFICATION AND STATISTICAL ANALYSIS

Biochemical experiments *in vitro* were routinely repeated at least three times, and the repeat number was increased according to effect size or sample variation. We estimated the sample size considering the variation and mean of the samples. No statistical method was used to predetermine sample size. No animals or samples were excluded from any analysis. Animals were randomly assigned groups for *in vivo* studies; no formal randomization method was applied when assigning animals for treatment. All western blotting experiments with quantification were performed a minimum of three times with independent biological samples and analyzed by ImageJ 1.52q. Statistical analyses were performed using GraphPad Prism 8. All tests and p values are provided in the corresponding figures or figure legends.

Supplementary Material

Refer to Web version on PubMed Central for supplementary material.

ACKNOWLEDGMENTS

We thank members of the Chio and Chang labs, Drs. Richard Baer, Adolfo Ferrando, Swarnali Acharyya (Columbia University Irving Medical Center), and Dr. David Tuveson (Cold Spring Harbor Laboratory) for helpful discussion. We thank Dr. Gijs R. van den Brink (University of Amsterdam) for sharing their Noggin-FC-expressing cells and Dr. Tuveson for sharing human organoids. We thank Dr. Hanina Hibshoosh (Columbia University) for the procurement of surgically resected PDA specimens. We thank A. Killiea and M. Fischer (UC Berkeley Tissue Culture Facility) and M. Salemi and B. Phinney (UC Davis Proteomics Core) for technical assistance, and H. Iwashita (UC Berkeley) for providing PG1-FM. We thank A. I. Nesvizhskii (University of Michigan) for assistance on MSFragger.

Funding:

This work was performed with the support of Columbia University Herbert Irving Comprehensive Cancer Center Flow Cytometry, Confocal and Specialized Microscopy, Small Animal Imaging, and Molecular Pathology Shared Resources (NIH/NCI Cancer Center Support Grant, P30-CA13696), UC Davis Proteomics Core (S10-OD21801), GCRC Metabolomics Innovation Resource (Dr. John R and Clara M. Fraser Memorial Trust, the Terry Fox Foundation, the Québec Breast Cancer Foundation), and the University of Nebraska Medical Center's Rapid Autopsy Program for Pancreas (P50CA127297, U01CA210240, P30CA36727, R50CA211462). Other support includes the Tang Distinguished Scholarship (D.H.), National Science Foundation Graduate Fellowship (A.H.C., DGE 1106400), National Institute of Health grants (R01-GM139245 to C.J.C., R01-CA240654 to I.I.C.C., and Division of Preclinical Innovation, National Center for Advancing Translational Research and the Center for Cancer

Research, NCI to C.J.T.), Novartis-Berkeley Center for Proteomics and Chemical Technologies (to C.J.C. and F.D.T.), Agilent Design Program (to C.J.C.), and Pershing Square Sohn Research Alliance (to I.I.C.C.).

REFERENCES

Anastasiou D, Poulogiannis G, Asara JM, Boxer MB, Jiang JK, Shen M, Bellinger G, Sasaki AT, Locasale JW, Auld DS, et al. (2011). Inhibition of pyruvate kinase M2 by reactive oxygen species contributes to cellular antioxidant responses. Science 334, 1278–1283. 10.1126/science.1211485. [PubMed: 22052977]

Anastasiou D, Yu Y, Israelsen WJ, Jiang JK, Boxer MB, Hong BS, Tempel W, Dimov S, Shen M, Jha A, et al. (2012). Pyruvate kinase M2 activators promote tetramer formation and suppress tumorigenesis. Nature chemical biology 8, 839–847. 10.1038/nchembio.1060. [PubMed: 22922757]

Bankhead P, Loughrey MB, Fernandez JA, Dombrowski Y, McArt DG, Dunne PD, McQuaid S, Gray RT, Murray LJ, Coleman HG, et al. (2017). QuPath: Open source software for digital pathology image analysis. Scientific reports 7, 16878. 10.1038/s41598-017-17204-5. [PubMed: 29203879]

Bergers G, and Fendt SM (2021). The metabolism of cancer cells during metastasis. Nat Rev Cancer 21, 162–180. 10.1038/s41568-020-00320-2. [PubMed: 33462499]

Birsoy K, Wang T, Chen WW, Freinkman E, Abu-Remaileh M, and Sabatini DM (2015). An Essential Role of the Mitochondrial Electron Transport Chain in Cell Proliferation Is to Enable Aspartate Synthesis. Cell 162, 540–551. 10.1016/j.cell.2015.07.016. [PubMed: 26232224]

Boj SF, Hwang CI, Baker LA, Chio II, Engle DD, Corbo V, Jager M, Ponz-Sarvise M, Tiriac H, Spector MS, et al. (2015). Organoid models of human and mouse ductal pancreatic cancer. Cell 160, 324–338. 10.1016/j.cell.2014.12.021. [PubMed: 25557080]

Caino MC, Ghosh JC, Chae YC, Vaira V, Rivadeneira DB, Faversani A, Rampini P, Kossenkov AV, Aird KM, Zhang R, et al. (2015). PI3K therapy reprograms mitochondrial trafficking to fuel tumor cell invasion. Proc Natl Acad Sci U S A 112, 8638–8643. 10.1073/pnas.1500722112. [PubMed: 26124089]

Caino MC, Seo JH, Aguinaldo A, Wait E, Bryant KG, Kossenkov AV, Hayden JE, Vaira V, Morotti A, Ferrero S, et al. (2016). A neuronal network of mitochondrial dynamics regulates metastasis. Nature communications 7, 13730. 10.1038/ncomms13730.

Cattaruzza M, and Hecker M (2008). Protein carbonylation and decarboylation: a new twist to the complex response of vascular cells to oxidative stress. Circulation research 102, 273–274. 10.1161/CIRCRESAHA.108.172148. [PubMed: 18276922]

Chambers MC, Maclean B, Burke R, Amodei D, Ruderman DL, Neumann S, Gatto L, Fischer B, Pratt B, Egertson J, et al. (2012). A cross-platform toolkit for mass spectrometry and proteomics. Nat Biotechnol 30, 918–920. 10.1038/nbt.2377. [PubMed: 23051804]

Chaneton B, and Gottlieb E (2012). Rocking cell metabolism: revised functions of the key glycolytic regulator PKM2 in cancer. Trends in biochemical sciences 37, 309–316. 10.1016/j.tibs.2012.04.003. [PubMed: 22626471]

Chaneton B, Hillmann P, Zheng L, Martin ACL, Maddocks ODK, Chokkathukalam A, Coyle JE, Jankevics A, Holding FP, Vousden KH, et al. (2012). Serine is a natural ligand and allosteric activator of pyruvate kinase M2. Nature 491, 458–462. 10.1038/nature11540. [PubMed: 23064226]

Chio II, Jafarnejad SM, Ponz-Sarvise M, Park Y, Rivera K, Palm W, Wilson J, Sangar V, Hao Y, Ohlund D, et al. (2016). NRF2 Promotes Tumor Maintenance by Modulating mRNA Translation in Pancreatic Cancer. Cell 166, 963–976. 10.1016/j.cell.2016.06.056. [PubMed: 27477511]

Christian AH, Jia S, Cao W, Zhang P, Meza AT, Sigman MS, Chang CJ, and Toste FD (2019). A Physical Organic Approach to Tuning Reagents for Selective and Stable Methionine Bioconjugation. J Am Chem Soc 141, 12657–12662. 10.1021/jacs.9b04744. [PubMed: 31361488]

Christofk HR, Vander Heiden MG, Harris MH, Ramanathan A, Gerszten RE, Wei R, Fleming MD, Schreiber SL, and Cantley LC (2008a). The M2 splice isoform of pyruvate kinase is important for cancer metabolism and tumour growth. Nature 452, 230–U274. 10.1038/nature06734. [PubMed: 18337823]

Christofk HR, Vander Heiden MG, Wu N, Asara JM, and Cantley LC (2008b). Pyruvate kinase M2 is a phosphotyrosine-binding protein. Nature 452, 181–186. 10.1038/nature06667. [PubMed: 18337815]

Dayton TL, Gocheva V, Miller KM, Israelsen WJ, Bhutkar A, Clish CB, Davidson SM, Luengo A, Bronson RT, Jacks T, and Vander Heiden MG (2016). Germline loss of PKM2 promotes metabolic distress and hepatocellular carcinoma. Genes Dev 30, 1020–1033. 10.1101/gad.278549.116. [PubMed: 27125672]

De Luca A, Sanna F, Sallese M, Ruggiero C, Grossi M, Sacchetta P, Rossi C, De Laurenzi V, Di Ilio C, and Favaloro B (2010). Methionine sulfoxide reductase A down-regulation in human breast cancer cells results in a more aggressive phenotype. Proc Natl Acad Sci U S A 107, 18628–18633. 10.1073/pnas.1010171107. [PubMed: 20937881]

DeNicola GM, Karreth FA, Humpton TJ, Gopinathan A, Wei C, Frese K, Mangal D, Yu KH, Yeo CJ, Calhoun ES, et al. (2011). Oncogene-induced Nrf2 transcription promotes ROS detoxification and tumorigenesis. Nature 475, 106–109. 10.1038/nature10189. [PubMed: 21734707]

Elias JE, and Gygi SP (2007). Target-decoy search strategy for increased confidence in large-scale protein identifications by mass spectrometry. Nat Methods 4, 207–214. 10.1038/nmeth1019. [PubMed: 17327847]

Elledge SK, Tran HL, Christian AH, Steri V, Hann B, Toste FD, Chang CJ, and Wells JA (2020). Systematic identification of engineered methionines and oxaziridines for efficient, stable, and site-specific antibody bioconjugation. Proc Natl Acad Sci U S A 117, 5733–5740. 10.1073/pnas.1920561117. [PubMed: 32123103]

Eng JK, Jahan TA, and Hoopmann MR (2013). Comet: an open-source MS/MS sequence database search tool. Proteomics 13, 22–24. 10.1002/pmic.201200439. [PubMed: 23148064]

Erickson JR, Joiner ML, Guan X, Kutschke W, Yang J, Oddis CV, Bartlett RK, Lowe JS, O'Donnell SE, Aykin-Burns N, et al. (2008). A dynamic pathway for calcium-independent activation of CaMKII by methionine oxidation. Cell 133, 462–474. 10.1016/j.cell.2008.02.048. [PubMed: 18455987]

Fang JX, Uchiumi T, Yagi M, Matsumoto S, Amamoto R, Takazaki S, Yamaza H, Nonaka K, and Kang DC (2013). Dihydro-orotate dehydrogenase is physically associated with the respiratory complex and its loss leads to mitochondrial dysfunction. Bioscience Rep 33, 217–227. ARTN e00021 10.1042/BSR20120097.

Gruning NM, Rinnerthaler M, Bluemlein K, Mulleder M, Wamelink MM, Lehrach H, Jakobs C, Breitenbach M, and Ralser M (2011). Pyruvate kinase triggers a metabolic feedback loop that controls redox metabolism in respiring cells. Cell Metab 14, 415–427. 10.1016/j.cmet.2011.06.017. [PubMed: 21907146]

Guminska M, Ignacak J, Kedryna T, and Stachurska MB (1997). Tumor-specific pyruvate kinase isoenzyme M2 involved in biochemical strategy of energy generation in neoplastic cells. Acta Biochim Pol 44, 711–724. [PubMed: 9584851]

Hingorani SR, Wang L, Multani AS, Combs C, Deramaudt TB, Hruban RH, Rustgi AK, Chang S, and Tuveson DA (2005). Trp53R172H and KrasG12D cooperate to promote chromosomal instability and widely metastatic pancreatic ductal adenocarcinoma in mice. Cancer Cell 7, 469–483. 10.1016/j.ccr.2005.04.023. [PubMed: 15894267]

Hitosugi T, Kang S, Vander Heiden MG, Chung TW, Elf S, Lythgoe K, Dong S, Lonial S, Wang X, Chen GZ, et al. (2009). Tyrosine phosphorylation inhibits PKM2 to promote the Warburg effect and tumor growth. Science signaling 2, ra73. 10.1126/scisignal.2000431. [PubMed: 19920251]

Hooda J, Cadinu D, Alam MM, Shah A, Cao TM, Sullivan LA, Brekken R, and Zhang L (2013). Enhanced heme function and mitochondrial respiration promote the progression of lung cancer cells. PloS one 8, e63402. 10.1371/journal.pone.0063402. [PubMed: 23704904]

Hsu PD, Scott DA, Weinstein JA, Ran FA, Konermann S, Agarwala V, Li Y, Fine EJ, Wu X, Shalem O, et al. (2013). DNA targeting specificity of RNA-guided Cas9 nucleases. Nature biotechnology 31, 827–832. 10.1038/nbt.2647.

Huch M, Bonfanti P, Boj SF, Sato T, Loomans CJ, van de Wetering M, Sojoodi M, Li VS, Schuijers J, Gracanin A, et al. (2013). Unlimited in vitro expansion of adult bi-potent pancreas progenitors through the Lgr5/R-spondin axis. The EMBO journal 32, 2708–2721. 10.1038/emboj.2013.204. [PubMed: 24045232]

Hung RJ, Pak CW, and Terman JR (2011). Direct redox regulation of F-actin assembly and disassembly by Mical. Science 334, 1710–1713. 10.1126/science.1211956. [PubMed: 22116028]

Israelsen WJ, Dayton TL, Davidson SM, Fiske BP, Hosios AM, Bellinger G, Li J, Yu Y, Sasaki M, Horner JW, et al. (2013). PKM2 isoform-specific deletion reveals a differential requirement for pyruvate kinase in tumor cells. Cell 155, 397–409. 10.1016/j.cell.2013.09.025. [PubMed: 24120138]

Israelsen WJ, and Vander Heiden MG (2015). Pyruvate kinase: Function, regulation and role in cancer. Semin Cell Dev Biol 43, 43–51. 10.1016/j.semcdb.2015.08.004. [PubMed: 26277545]

Iwashita H, Castillo E, Messina MS, Swanson RA, and Chang CJ (2021). A tandem activity-based sensing and labeling strategy enables imaging of transcellular hydrogen peroxide signaling. Proc Natl Acad Sci U S A 118. 10.1073/pnas.2018513118.

Jiang J, Walsh MJ, Brimacombe KR, Anastasiou D, Yu Y, Israelsen WJ, Hong BS, Tempel W, Dimov S, Veith H, et al. (2010). ML265: A potent PKM2 activator induces tetramerization and reduces tumor formation and size in a mouse xenograft model. In Probe Reports from the NIH Molecular Libraries Program.

Kanehisa M, Sato Y, Furumichi M, Morishima K, and Tanabe M (2019). New approach for understanding genome variations in KEGG. Nucleic acids research 47, D590–D595. 10.1093/nar/gky962. [PubMed: 30321428]

Kato M, Li J, Chuang JL, and Chuang DT (2007). Distinct structural mechanisms for inhibition of pyruvate dehydrogenase kinase isoforms by AZD7545, dichloroacetate, and radicicol. Structure 15, 992–1004. 10.1016/j.str.2007.07.001. [PubMed: 17683942]

Kato M, Yang YS, Sutter BM, Wang Y, McKnight SL, and Tu BP (2019). Redox State Controls Phase Separation of the Yeast Ataxin-2 Protein via Reversible Oxidation of Its Methionine-Rich Low-Complexity Domain. Cell 177, 711–721 e718. 10.1016/j.cell.2019.02.044. [PubMed: 30982603]

Kelley LC, Chi Q, Caceres R, Hastie E, Schindler AJ, Jiang Y, Matus DQ, Plastino J, and Sherwood DR (2019). Adaptive F-Actin Polymerization and Localized ATP Production Drive Basement Membrane Invasion in the Absence of MMPs. Developmental cell 48, 313–328 e318. 10.1016/j.devcel.2018.12.018. [PubMed: 30686527]

Kemper EK, Zhang Y, Dix MM, and Cravatt BF (2022). Global profiling of phosphorylation-dependent changes in cysteine reactivity. Nature methods. 10.1038/s41592-022-01398-2.

Kim HY, and Gladyshev VN (2004). Methionine sulfoxide reduction in mammals: characterization of methionine-R-sulfoxide reductases. Molecular biology of the cell 15, 1055–1064. 10.1091/mbc.e03-08-0629. [PubMed: 14699060]

Knott SRV, Wagenblast E, Khan S, Kim SY, Soto M, Wagner M, Turgeon MO, Fish L, Erard N, Gable AL, et al. (2018). Erratum: Asparagine bioavailability governs metastasis in a model of breast cancer. Nature 556, 135. 10.1038/nature26162.

Kong AT, Leprevost FV, Avtonomov DM, Mellacheruvu D, and Nesvizhskii AI (2017). MSFragger: ultrafast and comprehensive peptide identification in mass spectrometry-based proteomics. Nat Methods 14, 513–520. 10.1038/nmeth.4256. [PubMed: 28394336]

Krall AS, Mullen PJ, Surjono F, Momcilovic M, Schmid EW, Halbrook CJ, Thambundit A, Mittelman SD, Lyssiotis CA, Shackelford DB, et al. (2021). Asparagine couples mitochondrial respiration to ATF4 activity and tumor growth. Cell Metab 33, 1013–1026 e1016. 10.1016/j.cmet.2021.02.001. [PubMed: 33609439]

Kulawiec M, Owens KM, and Singh KK (2009). Cancer cell mitochondria confer apoptosis resistance and promote metastasis. Cancer Biol Ther 8, 1378–1385. 10.4161/cbt.8.14.8751. [PubMed: 19556849]

Lane AN, and Fan TW (2015). Regulation of mammalian nucleotide metabolism and biosynthesis. Nucleic acids research 43, 2466–2485. 10.1093/nar/gkv047. [PubMed: 25628363]

LeBleu VS, O'Connell JT, Gonzalez Herrera KN, Wikman H, Pantel K, Haigis MC, de Carvalho FM, Damascena A, Domingos Chinen LT, Rocha RM, et al. (2014). PGC-1alpha mediates mitochondrial biogenesis and oxidative phosphorylation in cancer cells to promote metastasis. Nat Cell Biol 16, 992–1003, 1001–1015. 10.1038/ncb3039. [PubMed: 25241037]

Lee BC, Peterfi Z, Hoffmann FW, Moore RE, Kaya A, Avanesov A, Tarrago L, Zhou Y, Weerapana E, Fomenko DE, et al. (2013). MsrB1 and MICALs regulate actin assembly and macrophage

function via reversible stereoselective methionine oxidation. Mol Cell 51, 397–404. 10.1016/j.molcel.2013.06.019. [PubMed: 23911929]

Lei KF, Wang YF, Zhu XQ, Lu PC, Sun BS, Jia HL, Ren N, Ye QH, Sun HC, Wang L, et al. (2007). Identification of MSRA gene on chromosome 8p as a candidate metastasis suppressor for human hepatitis B virus-positive hepatocellular carcinoma. BMC Cancer 7, 172. 10.1186/1471-2407-7-172. [PubMed: 17784942]

Lin S, Yang X, Jia S, Weeks AM, Hornsby M, Lee PS, Nichiporuk RV, Iavarone AT, Wells JA, Toste FD, and Chang CJ (2017). Redox-based reagents for chemoselective methionine bioconjugation. Science 355, 597–602. 10.1126/science.aal3316. [PubMed: 28183972]

Luo S, and Levine RL (2009). Methionine in proteins defends against oxidative stress. FASEB journal : official publication of the Federation of American Societies for Experimental Biology 23, 464–472. 10.1096/fj.08-118414. [PubMed: 18845767]

Macpherson JA, Theisen A, Masino L, Fets L, Driscoll PC, Encheva V, Snijders AP, Martin SR, Kleinjung J, Barran PE, et al. (2019). Functional cross-talk between allosteric effects of activating and inhibiting ligands underlies PKM2 regulation. eLife 8. ARTN e45068 10.7554/eLife.45068.

Mazurek S, Boschek CB, Hugo F, and Eigenbrodt E (2005). Pyruvate kinase type M2 and its role in tumor growth and spreading. Semin Cancer Biol 15, 300–308. 10.1016/j.semcancer.2005.04.009. [PubMed: 15908230]

McDonald WH, Tabb DL, Sadygov RG, MacCoss MJ, Venable J, Graumann J, Johnson JR, Cociorva D, and Yates JR 3rd (2004). MS1, MS2, and SQT-three unified, compact, and easily parsed file formats for the storage of shotgun proteomic spectra and identifications. Rapid Commun Mass Spectrom 18, 2162–2168. 10.1002/rcm.1603. [PubMed: 15317041]

Moffitt RA, Marayati R, Flate EL, Volmar KE, Loeza SG, Hoadley KA, Rashid NU, Williams LA, Eaton SC, Chung AH, et al. (2015). Virtual microdissection identifies distinct tumor- and stroma-specific subtypes of pancreatic ductal adenocarcinoma. Nat Genet 47, 1168–1178. 10.1038/ng.3398. [PubMed: 26343385]

Mookerjee SA, Gerencser AA, Nicholls DG, and Brand MD (2017). Quantifying intracellular rates of glycolytic and oxidative ATP production and consumption using extracellular flux measurements. Journal of Biological Chemistry 292, 7189–7207. 10.1074/jbc.M116.774471. [PubMed: 28270511]

Morgan B, Sobotta MC, and Dick TP (2011). Measuring E(GSH) and H2O2 with roGFP2-based redox probes. Free Radic Biol Med 51, 1943–1951. 10.1016/j.freeradbiomed.2011.08.035. [PubMed: 21964034]

Morita M, Sato T, Nomura M, Sakamoto Y, Inoue Y, Tanaka R, Ito S, Kurosawa K, Yamaguchi K, Sugiura Y, et al. (2018). PKM1 Confers Metabolic Advantages and Promotes Cell-Autonomous Tumor Cell Growth. Cancer Cell 33, 355–367 e357. 10.1016/j.ccell.2018.02.004. [PubMed: 29533781]

Moskovitz J, Berlett BS, Poston JM, and Stadtman ER (1997). The yeast peptide methionine sulfoxide reductase functions as an antioxidant in vivo. Proc Natl Acad Sci U S A 94, 9585–9589. DOI 10.1073/pnas.94.18.9585. [PubMed: 9275166]

Moskovitz J, Rahman MA, Strassman J, Yancey SO, Kushner SR, Brot N, and Weissbach H (1995). Escherichia coli peptide methionine sulfoxide reductase gene: regulation of expression and role in protecting against oxidative damage. Journal of bacteriology 177, 502–507. 10.1128/jb.177.3.502-507.1995. [PubMed: 7836279]

Nanchen A, Fuhrer T, and Sauer U (2007). Determination of metabolic flux ratios from 13C-experiments and gas chromatography-mass spectrometry data: protocol and principles. Methods Mol Biol 358, 177–197. 10.1007/978-1-59745-244-1_11.

Nie K, Li J, He X, Wang Y, Zhao Q, Du M, Sun H, Wang J, Lyu J, Fang H, and Jin L (2020). COX6B2 drives metabolic reprogramming toward oxidative phosphorylation to promote metastasis in pancreatic ductal cancer cells. Oncogenesis 9, 51. 10.1038/s41389-020-0231-2. [PubMed: 32415061]

Ohata J, Krishnamoorthy L, Gonzalez MA, Xiao T, Iovan DA, Toste FD, Miller EW, and Chang CJ (2020). An Activity-Based Methionine Bioconjugation Approach To Developing Proximity-Activated Imaging Reporters. ACS Cent Sci 6, 32–40. 10.1021/acscentsci.9b01038. [PubMed: 31989024]

Paulsen CE, and Carroll KS (2013). Cysteine-mediated redox signaling: chemistry, biology, and tools for discovery. Chemical reviews 113, 4633–4679. 10.1021/cr300163e. [PubMed: 23514336]

Piskounova E, Agathocleous M, Murphy MM, Hu Z, Huddlestun SE, Zhao Z, Leitch AM, Johnson TM, DeBerardinis RJ, and Morrison SJ (2015). Oxidative stress inhibits distant metastasis by human melanoma cells. Nature 527, 186–191. 10.1038/nature15726. [PubMed: 26466563]

Plubell DL, Wilmarth PA, Zhao Y, Fenton AM, Minnier J, Reddy AP, Klimek J, Yang X, David LL, and Pamir N (2017). suppded Multiplexing of Tandem Mass Tags (TMT) Labeling Reveals Age and High Fat Diet Specific Proteome Changes in Mouse Epididymal Adipose Tissue. Mol Cell Proteomics 16, 873–890. 10.1074/mcp.M116.065524. [PubMed: 28325852]

Porporato PE, Payen VL, Perez-Escuredo J, De Saedeleer CJ, Danhier P, Copetti T, Dhup S, Tardy M, Vazeille T, Bouzin C, et al. (2014). A mitochondrial switch promotes tumor metastasis. Cell reports 8, 754–766. 10.1016/j.celrep.2014.06.043. [PubMed: 25066121]

Rademaker G, Costanza B, Anania S, Agirman F, Maloujahmoum N, Di Valentin E, Goval JJ, Bellahcene A, Castronovo V, and Peulen O (2019). Myoferlin Contributes to the Metastatic Phenotype of Pancreatic Cancer Cells by Enhancing Their Migratory Capacity through the Control of Oxidative Phosphorylation. Cancers 11. ARTN 853 10.3390/cancers11060853.

Reczek CR, and Chandel NS (2017). The Two Faces of Reactive Oxygen Species in Cancer. Annu Rev Canc Biol 1, 79–98. 10.1146/annurev-cancerbio-041916-065808.

Rodrigues MF, Obre E, de Melo FH, Santos GC Jr., Galina A, Jasiulionis MG, Rossignol R, Rumjanek FD, and Amoedo ND (2016). Enhanced OXPHOS, glutaminolysis and beta-oxidation constitute the metastatic phenotype of melanoma cells. The Biochemical journal 473, 703–715. 10.1042/BJ20150645. [PubMed: 26699902]

Roe JS, Hwang CI, Somerville TDD, Milazzo JP, Lee EJ, Da Silva B, Maiorino L, Tiriac H, Young CM, Miyabayashi K, et al. (2017). Enhancer Reprogramming Promotes Pancreatic Cancer Metastasis. Cell 170, 875–888 e820. 10.1016/j.cell.2017.07.007. [PubMed: 28757253]

Salmeen A, and Barford D (2005). Functions and mechanisms of redox regulation of cysteine-based phosphatases. Antioxid Redox Signal 7, 560–577. 10.1089/ars.2005.7.560. [PubMed: 15890001]

Shaw RJ (2006). Glucose metabolism and cancer. Current opinion in cell biology 18, 598–608. 10.1016/j.ceb.2006.10.005. [PubMed: 17046224]

Shestov AA, Liu XJ, Ser Z, Cluntun AA, Hung YP, Huang L, Kim D, Le A, Yellen G, Albeck JG, and Locasale JW (2014). Quantitative determinants of aerobic glycolysis identify flux through the enzyme GAPDH as a limiting step. eLife 3. ARTN e03342 10.7554/eLife.03342.

Shi J, Wang E, Milazzo JP, Wang Z, Kinney JB, and Vakoc CR (2015). Discovery of cancer drug targets by CRISPR-Cas9 screening of protein domains. Nature biotechnology 33, 661–667. 10.1038/nbt.3235.

Singh MP, Kim KY, and Kim HY (2017). Methionine sulfoxide reductase A deficiency exacerbates acute liver injury induced by acetaminophen. Biochem Biophys Res Commun 484, 189–194. 10.1016/j.bbrc.2017.01.025. [PubMed: 28104395]

Smyth GK (2004). Linear models and empirical bayes methods for assessing differential expression in microarray experiments. Stat Appl Genet Mol Biol 3, Article3. 10.2202/1544-6115.1027. [PubMed: 16646809]

Stadtman ER, Moskovitz J, and Levine RL (2003). Oxidation of methionine residues of proteins: biological consequences. Antioxid Redox Signal 5, 577–582. 10.1089/152308603770310239. [PubMed: 14580313]

Sullivan LB, Gui DY, Hosios AM, Bush LN, Freinkman E, and Vander Heiden MG (2015). Supporting Aspartate Biosynthesis Is an Essential Function of Respiration in Proliferating Cells. Cell 162, 552–563. 10.1016/j.cell.2015.07.017. [PubMed: 26232225]

Tiriac H, Belleau P, Engle DD, Plenker D, Deschenes A, Somerville TDD, Froeling FEM, Burkhart RA, Denroche RE, Jang GH, et al. (2018). Organoid Profiling Identifies Common Responders to Chemotherapy in Pancreatic Cancer. Cancer Discov 8, 1112–1129. 10.1158/2159-8290.CD-18-0349. [PubMed: 29853643]

Wiel C, Le Gal K, Ibrahim MX, Jahangir CA, Kashif M, Yao H, Ziegler DV, Xu X, Ghosh T, Mondal T, et al. (2019). BACH1 Stabilization by Antioxidants Stimulates Lung Cancer Metastasis. Cell 178, 330–345 e322. 10.1016/j.cell.2019.06.005. [PubMed: 31257027]

Wilmarth PA, Riviere MA, and David LL (2009). Techniques for accurate protein identification in shotgun proteomic studies of human, mouse, bovine, and chicken lenses. J Ocul Biol Dis Infor 2, 223–234. 10.1007/s12177-009-9042-6. [PubMed: 20157357]

Yamaguchi N, Weinberg EM, Nguyen A, Liberti MV, Goodarzi H, Janjigian YY, Paty PB, Saltz LB, Kingham TP, Loo JM, et al. (2019). PCK1 and DHODH drive colorectal cancer liver metastatic colonization and hypoxic growth by promoting nucleotide synthesis. eLife 8. 10.7554/eLife.52135.

Zhang J, Wang X, Vikash V, Ye Q, Wu D, Liu Y, and Dong W (2016). ROS and ROS-Mediated Cellular Signaling. Oxid Med Cell Longev 2016, 4350965. 10.1155/2016/4350965. [PubMed: 26998193]

Zhou C, Sun H, Zheng C, Gao J, Fu Q, Hu N, Shao X, Zhou Y, Xiong J, Nie K, et al. (2018). Oncogenic HSP60 regulates mitochondrial oxidative phosphorylation to support Erk1/2 activation during pancreatic cancer cell growth. Cell death & disease 9, 161. 10.1038/s41419-017-0196-z. [PubMed: 29415987]

Highlights

- Methionine sulfoxide reductase (MSRA) suppresses pancreatic cancer metastasis
- Chemoproteomics identifies oxidation of PKM2 residue M239 in metastatic PDA cells
- PKM2-M239 oxidation sustains PKM2 in an active tetrameric state
- PKM2 activation promotes glucose oxidation and PDA metastasis

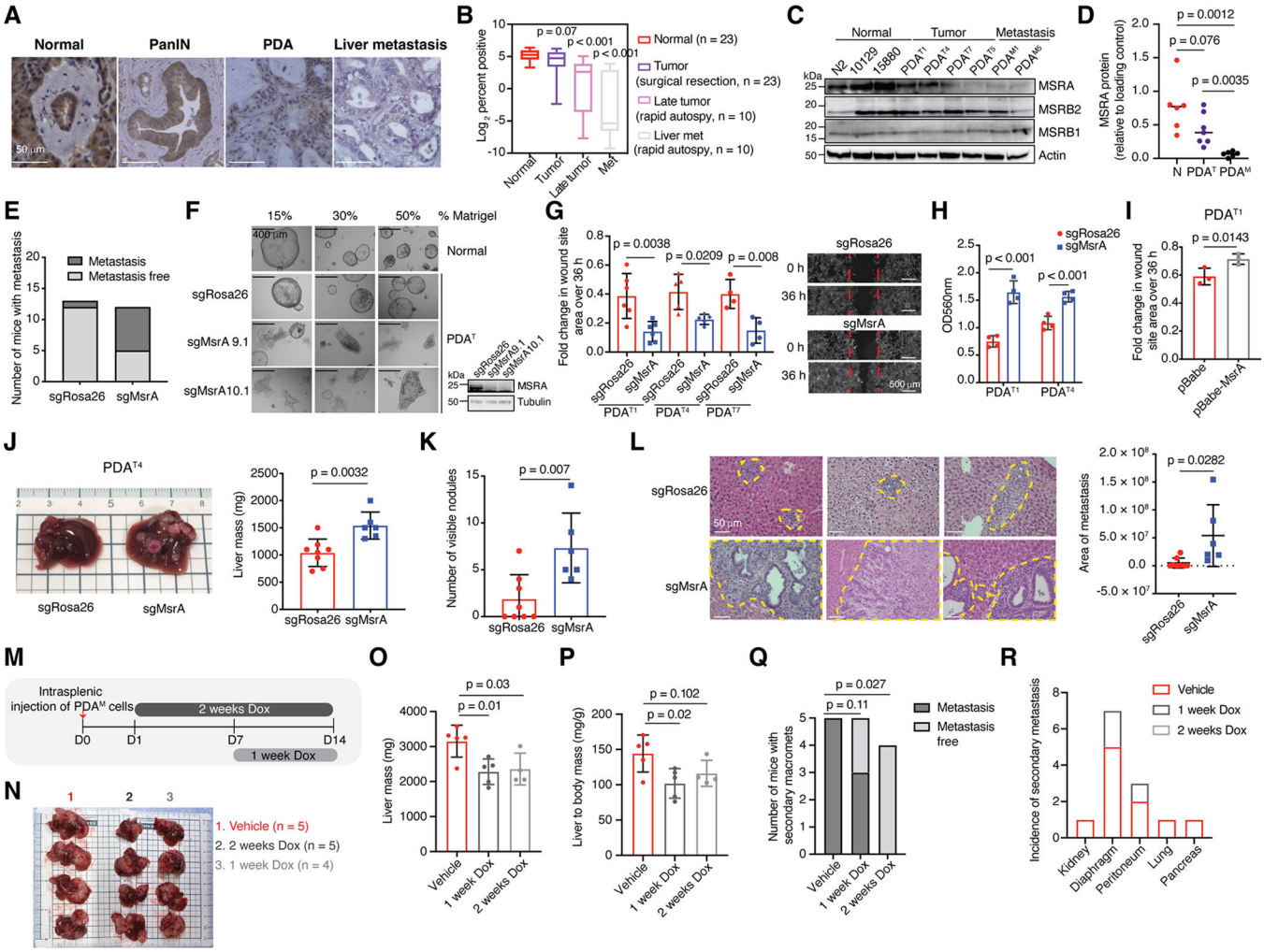

Figure 1. Methionine sulfoxide reductase A (MSRA) is a suppressor of pancreatic cancer metastasis

(A and B) Immunohistochemical staining (A) and quantification (B) of MSRA in patient-derived pancreatic tissues obtained from surgical resection (Normal, PanIN, PDA) or rapid autopsy (patient-matched PDA and liver metastasis). PanIN, pancreatic intraepithelial neoplasia. Data are min to max; lines indicate median.

(C and D) Immunoblot analysis of MSRA and MSRB proteins (C), and quantification of MSRA expression (D) in murine normal (n = 6), tumor (n = 7), and metastasis (n = 6) organoid lines; lines indicate median.

(E) Metastatic incidence of mice after orthotopic injection of PDA^{T4} cells expressing sgRosa26 (n = 13) or sgMsrA (n = 12).

(F) Brightfield images of pancreatic ductal organoids cultured in Matrigel for 96 hours. Immunoblot confirms the deletion of MSRA.

(G) Quantification and representative images of wound closure of PDA^{T} cells (n = 6, PDA^{T1}, n = 5, PDA^{T4}, n = 4, PDA^{T7}).

(H) Transwell migration of murine PDA^{T} cells (n = 4).

(I) Wound closure of murine PDA^{T} cells transduced with pBabe empty vector or pBabe-MsrA (n = 3).

(J-L) Liver colonization in mice after intrasplenic injection of PDA^{T}-sgRosa26 (n = 8) or PDA^{T}-sgMsrA9.1 (n = 6) cells. Liver mass (J), number of macroscopic lesions (K), and H&E staining analysis of liver micrometastases (demarcated by yellow contours) (L). Metastasis area was quantified using QuPath (Bankhead et al., 2017).
(M-R) Liver colonization in mice after intrasplenic injection of PDA^{M} expressing doxycycline-inducible MSRA and treated with vehicle (water) or doxycycline (10 mg/ml) by daily oral gavage. Experimental timeline (M) and representative images of livers (N). Liver mass (O), liver to body mass (P), number of mice with secondary macro-metastases (Q), and the organ distribution of metastasis (R).
All error bars are means ± SDs. Non-parametric Mann Whitney test was performed in (B), otherwise Student's *t*-test was performed.
See also Figure S1 and Table S1.

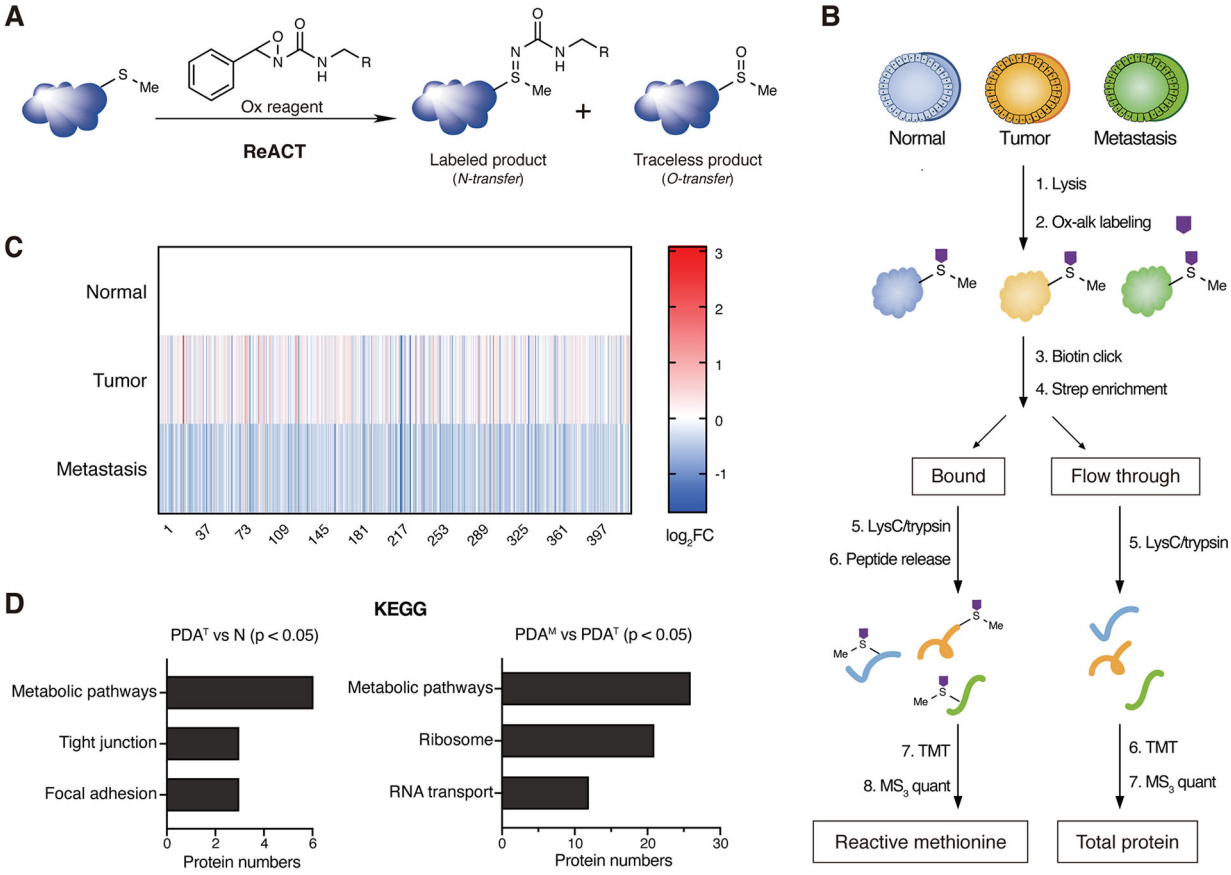

E

Proteins involved in central carbon metabolism

KO	Description	KO	Description
k00033	PGD; 6-phosphogluconate dehydrogenase	k02132	ATPeF1A; F-type H⁺-transporting ATPase subunit alpha
k00111	Gpd2; glycerol-3-phosphate dehydrogenase, mitocondrial	k02133	ATPeF1B; F-type H⁺-transporting ATPase subunit beta
k00234	SDHA; succinate dehydrogenase	k02136	ATPeF1G; F-type H⁺-transporting ATPase subunit gamma
k00235	SDHB; succinate dehydrogenase	k02145	ATPeV1A; V-type H⁺-transporting ATPase subunit A
k00873	PK; pyruvate kinase	k03934	NDUFS1; NADH dehydrogenase (ubiquinone) Fe-S protein 1
k01596	PCK; phosphoenolpyruvate carboxykinase (GTP)	k01834	PGAM; 2,3-bisphosphoglycerate-dependent phosphoglycerate mutase
k00658	DLST; 2-oxoglutarate dehydrogenase E2 component (dihydrolipoamide succinyltransferase)	k02261	COX2; cytochrome c oxidase subunit 2
k01647	CS; citrate synthase		
k01648	ACLY; ATP citrate (pro-S)-lyase		
k01681	ACO; aconitate hydratase		

Figure 2. Chemoproteomic profiling reveals enrichment of oxidation-sensitive methionine sites in metastatic pancreatic cancer organoid models

(A) Redox-Activated Chemical Tagging (ReACT) strategy for unbiased activity-based protein profiling and identification of oxidation-sensitive methionine sites in whole proteomes using oxaziridine (Ox)-based compounds.

(B) Schematic workflow of quantitative analysis of reactive methionine proteomes. TMT, tandem mass tag.

(C) Heatmap of activity-based, oxidation-sensitive methionine proteomes normalized to total proteome relative to normal organoids. FC, fold change.

(D) KEGG pathway analysis of significantly oxidized proteins in PDA^T organoids compared to normal (left) and PDA^M compared to PDA^T organoids (right) ($p < 0.05$, $q < 0.1$, *LIMMA* moderated *t* statistics). Top three pathways are shown.

(E) Table of proteins involved in central carbon metabolism that are significantly oxidized in PDA^M compared to PDA^T organoids.

See also Figure S2, Tables S2 to S4.

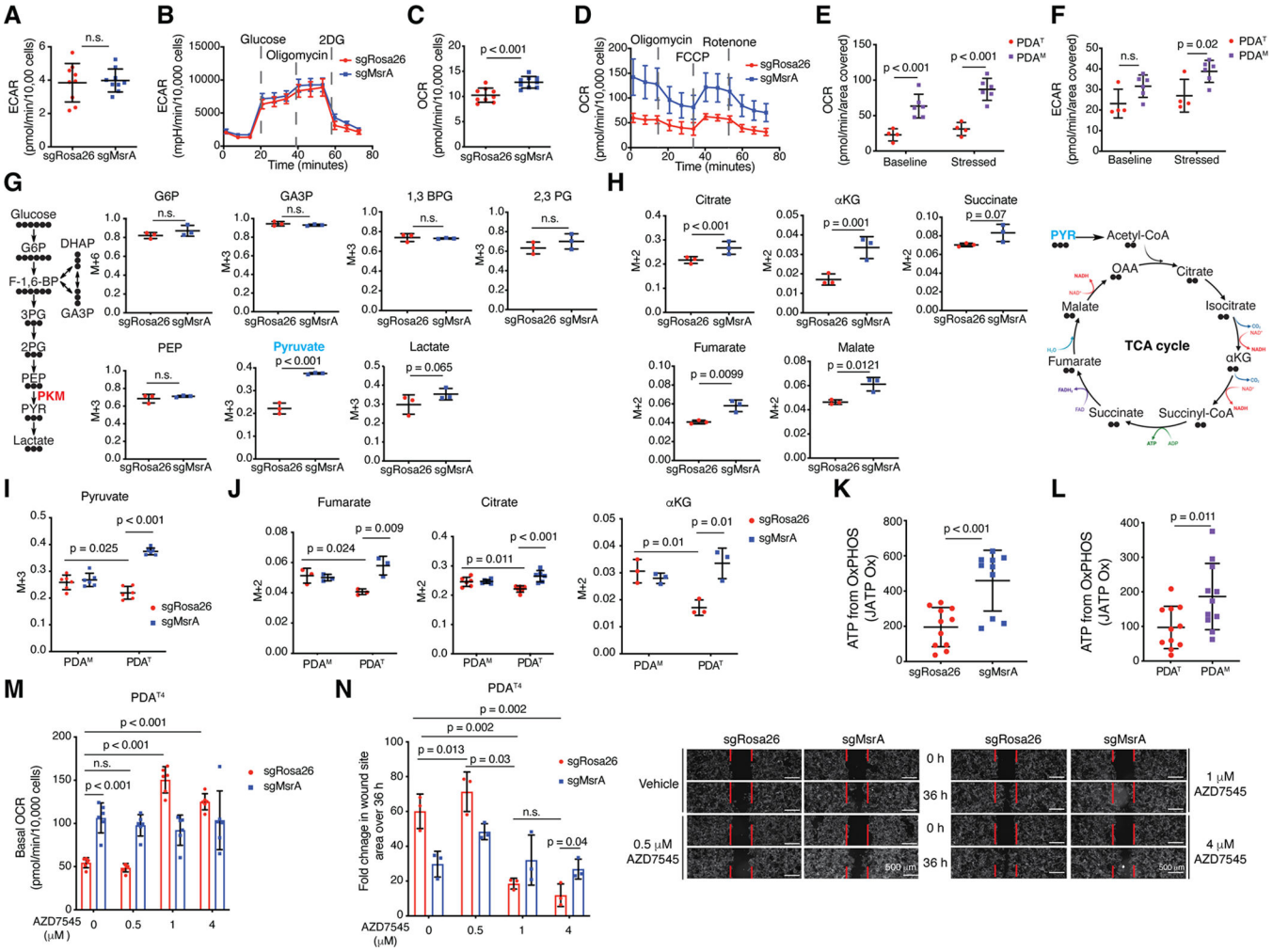

Figure 3. MSRA deficiency promotes glucose oxidation

(A to D) Glycolysis reflected by basal (A) and stressed (B) extracellular acidification rate (ECAR) and mitochondrial respiration reflected by basal (C) and stressed (D) oxygen consumption rate (OCR) in murine PDA^T cells. Data are normalized to cell number.

(E and F) OCR (E) and ECAR (F) in murine PDA^T (n = 4) and PDA^M (n = 6) organoids. Data normalized to total cell area.

(G and H) $^{13}C_6$-glucose tracing in murine PDA^T cells (n = 3) to determine the contribution of glucose to glycolysis (G) and TCA cycle intermediates (H). PKM, pyruvate kinase M.

(I and J) $^{13}C_6$-glucose tracing in murine $PDA^{T/M}$ cells to determine the contribution of glucose to pyruvate (n = 6) (I), fumarate (n = 3), citrate (n = 6) and αKG (n = 3) (J).

(K and L) ATP production quantified using this approach (Mookerjee et al., 2017) in murine PDA^T-sgRosa26 or PDA^T-sgMsrA cells (n = 10) (K), and in murine PDA^T and PDA^M organoids (n = 11) (L).

(M) OCR after 5 h treatment with vehicle (DMSO) or the indicated concentrations of AZD7545 (n = 6).

(N) Quantification and representative images of wound closure of murine PDA^T cells after vehicle (DMSO) or AZD7545 treatment (n = 3).

Error bars are all means ± SDs. In (A) and (C), n = 3 biological replicates and 3 technical replicates; (B) and (D), n = 5. Student's *t*-test was performed. n.s., not significant.
See also Figure S3.

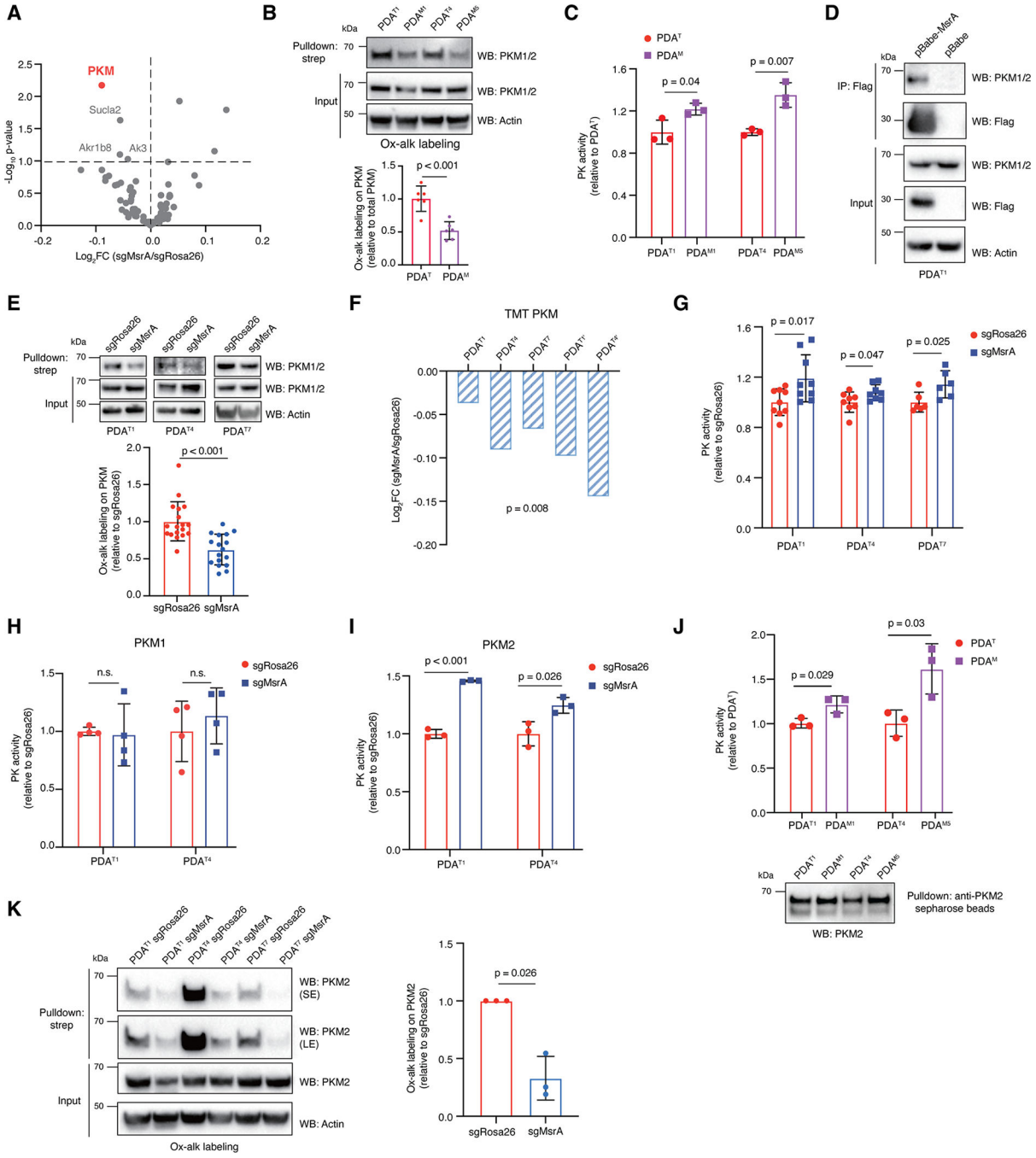

Figure 4. MSRA-dependent oxidation of PKM2 promotes pyruvate kinase activity

(A) Volcano plot of Ox-alkyne labeled metabolic proteins in PDA^{T}-sgMsrA compared to PDA^{T}-sgRosa26 cells. FC, fold change; one sample *t*-test (n = 3). Red circle, PKM.

(B and C) Immunoblot analysis of PKM methionine oxidation (n = 6) (B) and pyruvate kinase activity (n = 3) (C) in paired murine PDA^{T} and PDA^{M} cells. Actin, loading control.

(D) Immunoprecipitation of Myc-Flag tagged MSRA stably expressed in PDA^{T} cells to evaluate PKM interaction. IP, immunoprecipitation.

(E and F) Immunoblot (E) and quantitative mass spectrometry (F) analysis of PKM methionine oxidation by Ox-alkyne labeling in murine PDA^T cells. Quantification results in (E) pooled from all three lines (n = 18, sgRosa26, n = 17, sgMsrA). TMT, tandem mass tag.

(G) Pyruvate kinase activity of murine PDA^T cells. Data normalized to total protein content. (n = 9, PDA^{T1}, n = 8, PDA^{T4}, n = 6, PDA^{T7}).

(H and I) Pyruvate kinase activity of immunopurified PKM1 (n = 4) (H) or PKM2 (n = 3) (I) in murine PDA^T cells stably expressing either isoform.

(J) Pyruvate kinase activity of immunopurified endogenous PKM2 from PDA^T and PDA^M cells. Activity was normalized to relative PKM2 protein expression analyzed by immunoblotting (n = 3).

(K) Immunoblot analysis of PKM2 methionine oxidation by Ox-alkyne labeling of murine PDA^T-sgRosa26 or PDA^T-sgMsrA cells (n = 3). SE, short exposure; LE, long exposure. Data in (F) are individual $\log_2$ FC value from each sample, $PDA^{T1'}$ and $PDA^{T4'}$ are technical replicates. All error bars are means ± SDs. Student's *t*-test was performed, except in (A) and (F) one sample *t*-test was performed. n.s., not significant.

See also Figure S4.

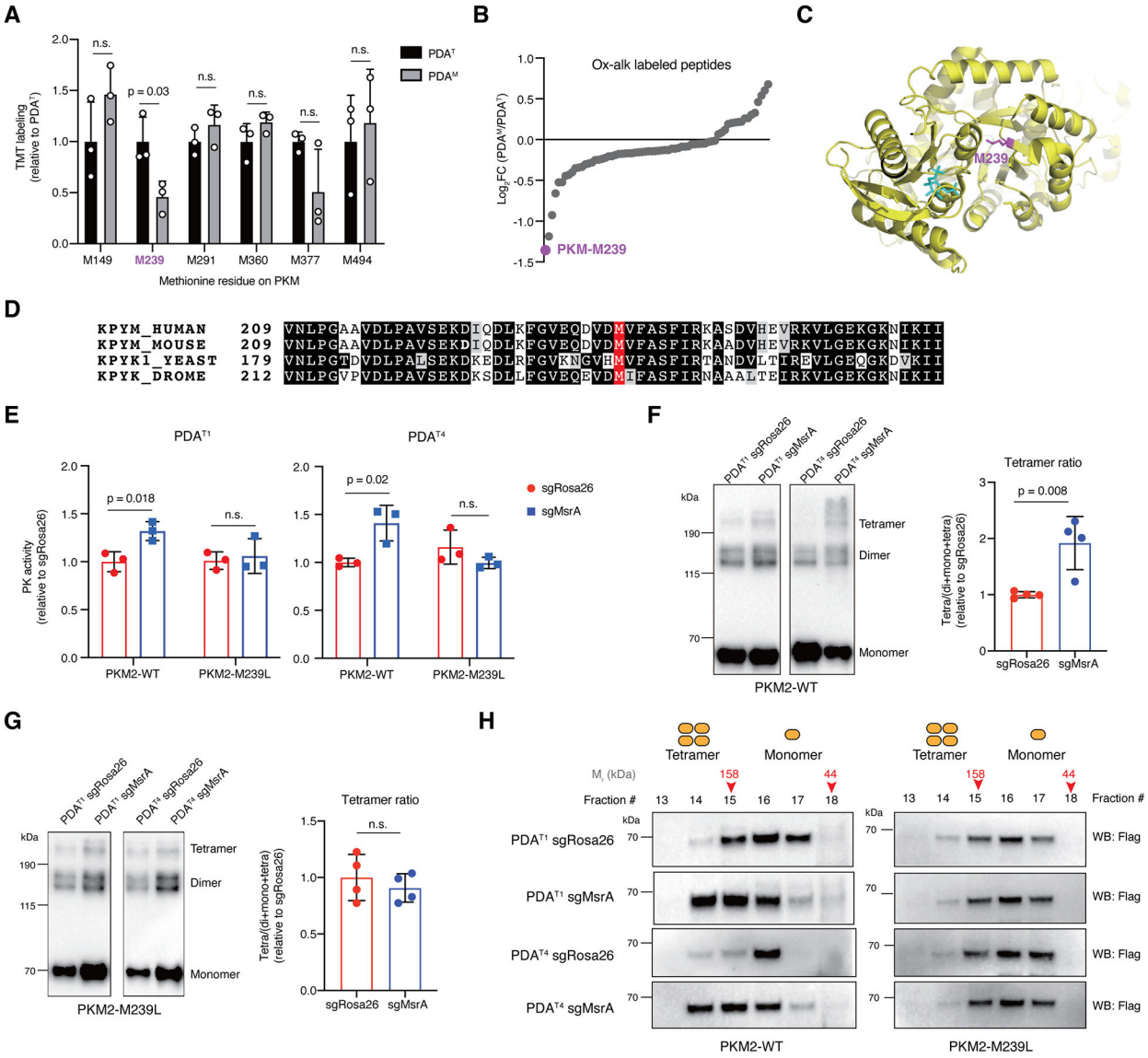

Figure 5. Site-specific oxidation of PKM2 at allosteric M239 site promotes tetramer formation

(A) Quantitative mass spectrometric analysis of Ox-alkyne labeled methionine residues on PKM in PDA^T and PDA^M organoids (n = 3).

(B) Ranked log$_2$FC of Ox-alkyne labeled peptides in murine PDA^T and PDA^M organoids by quantitative mass spectrometry. FC, fold change.

(C) Crystal structure of PKM2 (PDB 1T5A) showing the relative location of M239 to fructose 1,6-bisphosphate (cyan).

(D) Sequence alignment of *S. cerevisiae*, *D. melanogaster*, *Mus musculus* and *Homo sapiens* PKM2. Red residue, M239 in human/mouse sequence.

(E) Pyruvate kinase activity of immunopurified wild-type (WT) or M239L PKM2 from murine PDA^T cells stably expressing either construct (n = 3).

(F and G) Immunoblot analysis of the oligomeric state of immunopurified and crosslinked PKM2 wild-type (F) or M239L (G) proteins ectopically expressed in PDA^T cells. Quantification results pooled from two murine PDA^T cell lines (n = 4).

(H) Size exclusion chromatography analysis of murine PDA^T cells stably expressing PKM2-WT or PKM2-M239L.

All error bars are means ± SDs, except in (A) are means + SDs. Student's *t*-test was performed. n.s., not significant.

See also Figure S5 and Table S4.

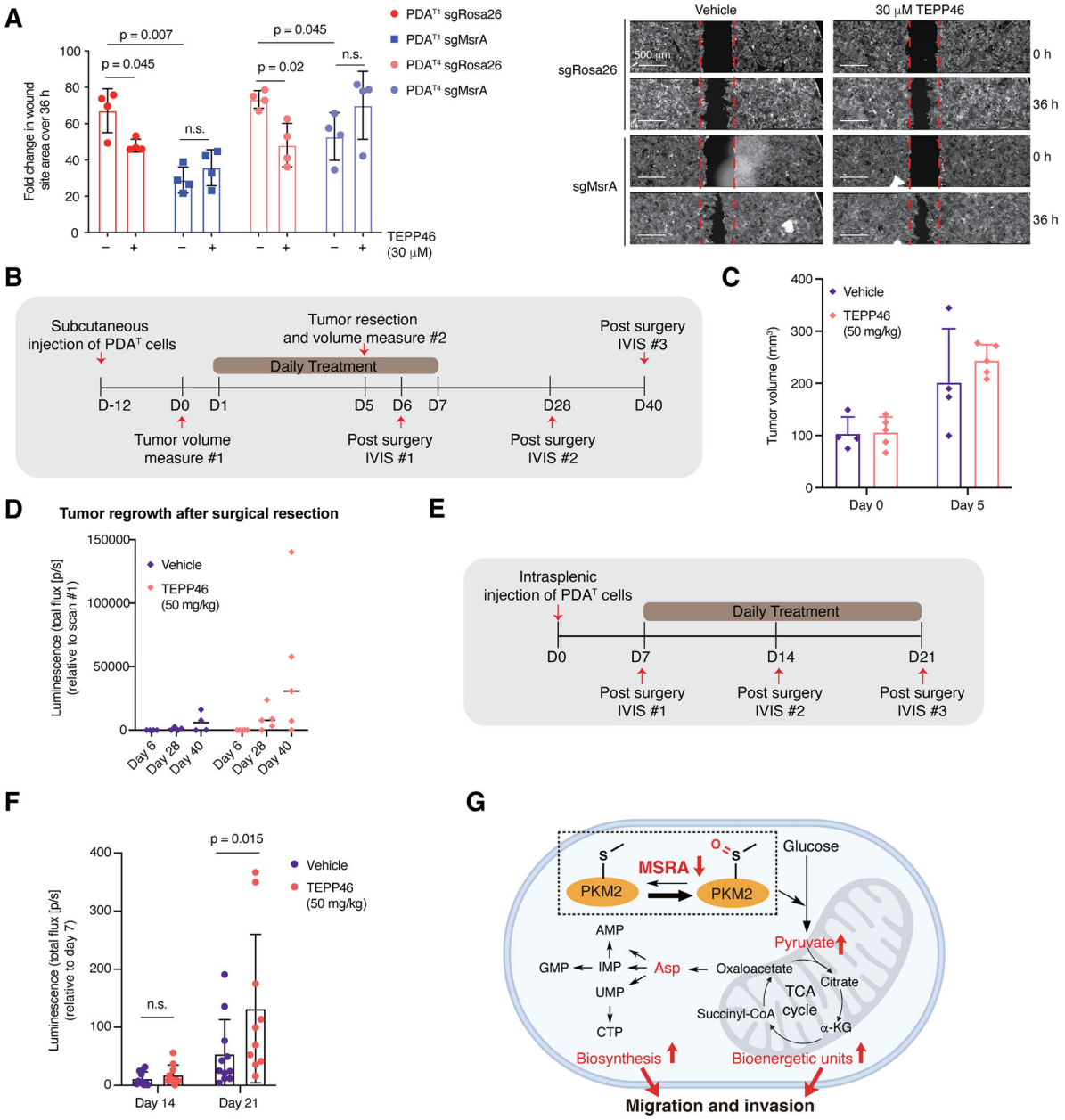

Figure 6. Activation of PKM2 promotes PDA metastasis

(A) Quantification and representative images of wound closure over 36 hours of PDA^T cells in the presence of vehicle (DMSO) or 30 μM TEPP46 (n = 4).

(B-D) Experimental timeline of TEPP46 treatment (B), tumor volume measured by calipers (C) and tumor regrowth measured by bioluminescence (D) in mice that received subcutaneous implantation of luciferase expressing PDA^T cells. Mice were treated with vehicle (n = 4) or 50 mg/kg TEPP46 (n = 5) twice a day.

(E and F) Experimental timeline of TEPP46 treatment (E) and liver colonization measured by bioluminescence (F) in mice after intrasplenic injection of luciferase expressing PDA^T cells. Mice were treated with vehicle (n = 13) or 50 mg/kg TEPP46 (n = 12) twice a day.

(G) Working model depicting metabolic reprogramming upon MSRA loss to promote pancreatic cancer cell migration.

All error bars are means ± SDs, except in (C) are means + SDs. Student's *t*-test was performed. n.s., not significant.

See also Figure S6.

KEY RESOURCES TABLE

REAGENT or RESOURCE	SOURCE	IDENTIFIER
Antibodies		
MSRA	Invitrogen	Cat# PA5-88562, RRID:AB_2804997
MSRA	Sigma Prestige	Cat#HPA053069, RRID:AB_2682032
MSRB1	ThermoFisher	Cat#LF-PA0088, RRID:AB_2285669
MSRB1	Sigma Prestige	Cat#HPA069557, RRID:AB_2686153
MSRB2	ThermoFisher	Cat#PA5-99072, RRID:AB_2813685
PKM1/2	Cell Signaling Technology	Cat#3190, RRID:AB_2163695
PKM1	Cell Signaling Technology	Cat#7067, RRID:AB_2715534
PKM2	Cell Signaling Technology	Cat#4053, RRID:AB_1904096
Vinculin	Cell Signaling Technology	Cat#4650, RRID:AB_10559207
Vinculin	Sigma-Aldrich	Cat#V9131, RRID:AB_477629
Tubulin	Cell Signaling Technology	Cat#2148, RRID:AB_2288042
Actin	Cell Signaling Technology	Cat#8456, RRID:AB_10998774
V5 tag	EMD Millipore	Cat#AB3792, RRID:AB_91591
Flag M2 tag	Sigma-Aldrich	Cat#F1804, RRID:AB_262044
Myc tag	Cell Signaling Technology	Cat#2276, RRID:AB_331783
GAPDH	Cell Signaling Technology	Cat#2118, RRID:AB_561053
PGK1	Invitrogen	Cat#PA5-28612, RRID:AB_2546088
Phospho-p44/42 MAPK (T202/Y204)	Cell Signaling Technology	Cat#9101, RRID:AB_331646
P44/42 MAPK	Cell Signaling Technology	Cat#4695, RRID:AB_390779
Phospho-STAT3 (Y705)	Cell Signaling Technology	Cat#9145, RRID:AB_2491009
STAT3	Cell Signaling Technology	Cat#9139, RRID:AB_331757
Phospho-SMAD3 (S423/425)	Cell Signaling Technology	Cat#9520, RRID:AB_2193207
SMAD3	Cell Signaling Technology	Cat#9513, RRID:AB_2286450
Phospho-AKT (S473)	Cell Signaling Technology	Cat#4060, RRID:AB_2315049
AKT	Cell Signaling Technology	Cat#4685, RRID:AB_2225340
Phospho-FAK (Y397)	Cell Signaling Technology	Cat#8556, RRID:AB_10891442
Phospho-FAK (Y576/577)	Cell Signaling Technology	Cat#3281, RRID:AB_331079
Phospho-FAK (Y925)	Cell Signaling Technology	Cat#3284, RRID:AB_10831810
FAK	Cell Signaling Technology	Cat#13009, RRID:AB_2798086
Phospho-AMPKa (T172)	Cell Signaling Technology	Cat#4188, RRID:AB_2169396
AMPKa	Cell Signaling Technology	Cat#5831, RRID:AB_10622186
Phosph-p70 S6 kinase (T389)	Cell Signaling Technology	Cat#9234, RRID:AB_2269803
p70 S6 kinase	Cell Signaling Technology	Cat#2708, RRID:AB_390722
Streptavidin-HRP conjugate	Jackson ImmunoResearch	Cat#016-030-084, RRID:AB_2337238
Anti-cysteine sulfenic acid	Millipore	Cat#07-2139-I-25UL, RRID:AB_1977145
PKM2 mAb sepharose bead conjugate	Cell Signaling Technology	Cat#13266, RRID:AB_2798165

REAGENT or RESOURCE	SOURCE	IDENTIFIER
Anti 4-hydroxynonenal (HNE)	Alpha Diagnostic International	Cat#HNE11-S, RRID:AB_2629282
ATP5A	Abcam	Cat#ab14748, RRID:AB_301447
Histone H3	Cell Signaling Technology	Cat#4499, RRID:AB_10544537
Biological samples		
Human pancreatic tumor and metastatic specimens	University of Nebraska Medical Center's Rapid Autopsy Program for Pancreas	N/A
Deidentified human pancreatic tumor and adjacent normal specimens	Herbert Irving Comprehensive Cancer Center (HICCC) Tissue Bank	N/A
Chemicals, peptides, and recombinant proteins		
TMT10plex Isobaric label reagent	ThermoFisher Scientific	Cat#90110
Trypsin/Lysine-C protease mix	ThermoFisher Scientific	Cat#A41007
1M TEAB	ThermoFisher Scientific	Cat#90114
Adenosine 5'-diphosphate sodium salt	Sigma-Aldrich	Cat#A2754
Phospho(enol)pyruvic acid monopotassium salt	Sigma-Aldrich	Cat#P7127
anti-Flag M2 magnetic beads	Sigma-Aldrich	Cat#M8823
3 × Flag peptide	Sigma-Aldrich	Cat#F4799
Native lysis buffer	Abcam	Cat#ab156035
DYn-2	Cayman Chemical	Cat#11220
Iodoacetamide-alkyne	Oakwood Chemical	Cat#95226
Dimedone	Sigma-Aldrich	Cat#D153303
50% glutaraldehyde	Alfa Aesar	Cat#A10500
L-Aspartate	Genaxxon Bioscience	Cat#M6092.0250
Oligomycin-A	Sigma-Aldrich	Cat#75351
ML-265 (TEPP46)	Selleckchem	Cat#S7302
ML-265 (TEPP46)	Cayman Chemical	Cat#13942
AZD7545	Cayman Chemical	Cat#19282
Rotenone	Millipore	Cat#557368
FCCP	Sigma-Aldrich	Cat#C2920
2DG	Alfa Aesar	Cat#AAL0733806
Paraformaldehyde	Electron Microscopy Sciences	Cat#15710
N-ethylmaleimide (NEM)	Sigma-Aldrich	Cat#E3876
Dichloromethane	Fisher Scientific	Cat#D151-1
LC/MS grade methanol	Sigma-Aldrich	Cat#900688
LC/MS grade H_2O	Sigma-Aldrich	Cat#900682
Phalloidin FITC conjugate (reconstituted in methanol to 200U/ml)	Biotium	Cat#00030
D-luciferin	Goldbio	Cat#LUCK
Carboxymethylcellulose	Sigma-Aldrich	Cat#C5678
Tween80	Sigma-Aldrich	Cat#P1754
Nutlin-3a	Sigma-Aldrich	Cat#SML0580-5MG
Glucose	Sigma-Aldrich	Cat#G7021-100G

REAGENT or RESOURCE	SOURCE	IDENTIFIER
$^{13}C_6$-Glucose	Cambridge Isotope Laboratories	Cat#CLM -1396-PK
Carprofen	RIMADYL NADA	Cat#41-199
X-tremeGENE9	Sigma-Aldrich	Cat#6365787001
Polybrene	Millipore	Cat#TR1003G
Lipofectamine RNAiMAX transfection reagent	Invitrogen	Cat#13778075
Lipofectamine 2000 transfection reagent	Invitrogen	Cat#11668027
jetOPTIMUS	Polyplus	Cat#101000025
TEPP46	(Jiang et al., 2010)	Craig J. Thomas lab
PG1-FM	(Iwashita et al., 2021)	Christopher J. Chang lab
Methoxyamine hydrochloride	Sigma-Aldrich	Cat#226904
N-tert-Butyldimethylsilyl-*N*-methyltrifluoroacetamide (MTBSTFA)	Sigma	Cat#M-108
MitoTracker green FM	Cell Signaling Technology	Cat#9074
Hygromycin	Fisher Scientific	Cat#10687010
Antimycin A	Sigma-Aldrich	Cat#A8674-25MG
MitoTempo	Cayman Chemical	Cat#16621
N-acetyl-L-cysteine	Sigma-Aldrich	Cat#A9165-25G
L-Asparagine	Sigma-Aldrich	Cat#A4159-25G
Critical commercial assays		
Kinase-Glo plus luminescent kinase assay	Promega	Cat#V3771
Pyruvate kinase activity assay kit	Sigma-Aldrich	Cat#MAK072
NADP/NADPH colorimetric assay kit	BioVision	Cat#k347
Aspartate colorimetric/fluorometric assay kit	BioVision	Cat#K552
CellTiter-Glo	Promega	Cat#G7572
Protein carbonyl assay kit	Abcam	Cat#ab178020
BCA protein assay kit	Thermo Scientific	Cat#23227
QCM ECMatrix Cell Invasion Assay	Sigma-Aldrich	Cat#ECM550
Peptide fluorescent quantification kit	Thermo Scientific	Cat#23290
Cell Fractionation Kit	Abcam	Cat#ab109719
Deposited data		
Reactive methionine profiling	This study	MSV000089315
Glucose tracing	This study	MSV000089514
Experimental models: Cell lines		
Human: HEK293T	ATCC	Cat# CRL-3216, RRID:CVCL_0063
Mouse: KPC derived PDAC organoids	This study	N/A
Mouse: KPC derived PDAC cell lines	This study	N/A
Human: Phoenix-ECO	ATCC	Cat#CRL-3214, RRID:CVCL_H717
Experimental models: Organisms/strains		
Mouse: C57BL/6J	Jackson Laboratories	Stock#000664, IMSR_JAX:000664
Mouse: $Kras^{+/LSL-G12D}$	Jackson Laboratories	Stock#008179, IMSR_JAX:008179

REAGENT or RESOURCE	SOURCE	IDENTIFIER
Mouse: $p53^{+/LSL-R172H}$	Jackson Laboratories	Stock#008652, IMSR_JAX:008652
Mouse: Pdx1-Cre	Jackson Laboratories	Stock#014647, IMSR_JAX:014647
Oligonucleotides		
gRNA targeting MSRA (sgMsrA9.1): CACCGTACACAACCCGGACGACTT	This study	N/A
gRNA targeting MSRA (sgMsrA10.1): AAACCCGTGCAGATGGAAGCAGCC	This study	N/A
gRNA targteting ROSA locus (sgRosa26): GAAGATGGGCGGGAGTCTTC	This study	N/A
siRNA targeting human MsrA	Dharmacon	Cat#L-012464-00-0005
p53 loxP Fw: 5'AGCCTGCCTAGCTTCCTCAGG	This study	N/A
p53 loxP Rv: 5'CTTGGAGACATAGCCACACTG	This study	N/A
Recombinant DNA		
hMsrA-Myc-Flag-pCMV6-entry	Origene	Cat# RC208916
hMsrA-Myc-pCMV6-entry	This study	N/A
hMsrA-Myc-Flag-pBABE-puro	This study	N/A
mMsrA-Myc-Flag-pCMV6-entry	Origene	Cat#MR202816
mMsrA-Myc-Flag-pBABE-puro	This study	N/A
hPKM1-Flag-pCDNA3.1(+)	This study	N/A
mPKM1-V5-pBABE-neo	This study	N/A
hPKM2-Flag-pCDNA3.1 (+)	This study	N/A
mPKM2-Flag-pBABE-neo	This study	N/A
EFS-Cas9-P2A-Puro	Addgene	Addgene#108100
roGFP2-Orp1	(Morgan et al., 2011)	Tobias Dick lab
Mito-roGFP-Orp1	(Morgan et al., 2011)	Tobias Dick lab
Grx1-roGFP2	(Morgan et al., 2011)	Tobias Dick lab
Mito-Grx1-roGFP2	(Morgan et al., 2011)	Tobias Dick lab
Software and algorithms		
ImageJ	National Institutes of Health	https://imagej.nih.gov/ij/, RRID:SCR_003070
GraphPad Prism	GraphPad	http://www.graphpad.com/, RRID:SCR_002798
ChemBioDraw 13.0	PerkinElmer	https://www.perkinelmer.com/category/chemdraw, RRID:SCR_016768
Agilent MassHunter Quant software	Agilent Technologies	https://www.agilent.com/en/promotions/masshunter-mass-spec, RRID:SCR_015040
PAW (Proteomic Analysis Workflow) pipeline	(Wilmarth et al., 2009)	https://github.com/pwilmart/PAW_pepeline
Limma package	(Smyth, 2004)	https://bioconductor.org/packages/release/bioc/html/limma.html
MSFragger	(Kong et al., 2017)	https://msfragger.nesvilab.org/
QuPath	(Bankhead et al., 2017)	https://qupath.github.io/, RRID:SCR_018257

REAGENT or RESOURCE	SOURCE	IDENTIFIER
FlowJo	BD	https://www.flowjo.com/ RRID:SCR_008520
Vevo Lab 2.2.1	Fujifilm VisualSonics	https://www.visualsonics.com/product/software/vevo-lab RRID:SCR_015816
Living Image	Perkin Elmer	https://www.perkinelmer.com/category/image-analysis-software RRID:SCR_014247
Aperio Cytoplasm algorithm	Leica Biosystems	https://www.leicabiosystems.com/us/digital-pathology/analyze/ihc/aperio-cytoplasm-algorithm/ RRID:SCR_021016